

Bachelor's Thesis

Neutrinoerkennung durch maschinelles Lernen in der Suche nach Higgs-Paarproduktion im $bbWW^*$ -Endzustand am ATLAS-Experiment

Neutrino reconstruction using machine learning techniques for the boosted resonant $HH \rightarrow bbWW^*$ search at ATLAS

prepared by

Yannik Buch

from Soltau

at the II. Physikalisches Institut

Thesis number: II.Physik-UniGö-BSc-2020/07

Thesis period: 11th May 2020 until 31st August 2020

First referee: Prof. Dr. Stan Lai

Second referee: Prof. Dr. Ariane Frey

Zusammenfassung

Diese Bachelorarbeit präsentiert Neutrino-Rekonstruktionen mittels neuronaler Netzwerke. Die Neutrino-Rekonstruktion wird im resonanten $HH \rightarrow bbWW^*$ Kanal mit einem Lepton im Endzustand und geboosterter Topologie durchgeführt. Die Daten für diese Analyse stammen von Simulationen, die auf dem ATLAS Experiment am CERN beruhen. Motiviert ist diese Arbeit von der Suche nach skalaren Teilchen außerhalb des Standardmodells mit einer Masse zwischen 0.8 TeV und 5 TeV. Die Aufgabe des neuronalen Netzwerks ist hierbei eine Abschätzung für die z -Komponente des Neutrinoimpulses zu generieren, sodass die invariante Masse von $H \rightarrow WW^*$, m_H , und $X \rightarrow HH$, m_{HH} , rekonstruiert werden können. Das neuronale Netzwerk benutzt dafür die kinematischen Informationen von den messbaren Objekten des Endzustandes. Da dies der erste Einsatz eines neuronalen Netzwerks in diesem Kanal mit dieser Topologie ist, beginnt diese Arbeit mit der Messung einfacher Konfigurationen, um die Nutzbarkeit festzustellen. Danach werden mehrere Möglichkeiten zur Verbesserung der Präzision des neuronalen Netzwerks überprüft und vorgestellt. Die finale Konfiguration der Analyse verwendet ein einziges neuronales Netzwerk für die komplette Spanne der untersuchten Massen und liefert gute Ergebnisse für die Rekonstruktion von m_{HH} und besonders gute Ergebnisse für die Rekonstruktion von $m_{H \rightarrow WW^*}$.

Stichwörter: Physik, Bachelorarbeit, ATLAS, Neutrino Rekonstruktion, resonante Higgs Paarproduktion, Neuronale Netzwerke

Abstract

This Bachelor's thesis presents studies of neutrino reconstruction with neural networks. The analysis is conducted in the boosted resonant $HH \rightarrow bbWW^*$ channel with one lepton in the final state using simulated data. This thesis motivated by the search for particles beyond the Standard Model with the ATLAS collaboration. The search is conducted for heavy scalar particles with masses between 0.8 TeV and 5 TeV that decay into a pair of Higgs bosons. For this analysis, a full event reconstruction is strived for, but the kinematic information of the neutrino gathered from measurements are not complete. The neural networks task is to give an estimate of the neutrino's momentum in the z -direction p'_z as this quantity cannot be measured such that the invariant mass of $H \rightarrow WW^*$, m_H , and the invariant mass of $X \rightarrow HH$, m_{HH} , may be reconstructed. The neural network uses the kinematic information of the measurable particles in the final state to approximate p'_z . In the following, various possibilities to increase the performance are explored and presented. The final configuration relies on a single neural network that is trained and applied on the entire mass range. The resulting configuration of the neural network yields very good reconstruction of m_{HH} as well as $m_{H \rightarrow WW^*}$ using the approximated p'_z and improves on prior analyses that used $p'_z = 0$ when performing the event reconstruction.

Keywords: Physics, Bachelor thesis, ATLAS, neutrino reconstruction, resonant Higgs pair production, neural network

Contents

1. Introduction	1
2. Theoretical background	3
2.1. The Standard Model	3
2.1.1. The Higgs mechanism	5
2.1.2. The Higgs boson and Higgs boson pair production	7
2.2. Extensions of the Standard Model	10
3. The Large Hadron Collider and the ATLAS experiment	11
3.1. The CERN accelerator complex	11
3.2. The ATLAS experiment	12
4. Neural networks	17
4.1. The theory of neural networks	17
4.2. Application of the neural network	18
5. Analysis	23
5.1. Measures	23
5.2. Single mass point training	24
5.3. Training on multiple mass points	25
5.4. Input variables	28
5.5. Differentiation for on-shell and off-shell W bosons	30
5.6. Neural network optimizer	32
5.7. Neural network hyperparameters	36
5.8. Evaluation on background	36
6. Conclusion and Outlook	39
A. Figures	41
A.1. Distributions for native pairings and training on single mass points	41
A.2. Distributions for non-native pairings and training on single mass points . .	42

Contents

A.3. Distributions for training on multiple mass points	45
A.4. Distributions for the differentiation for on- and off-shell W bosons	49
B. Tables	51
B.1. Signal samples	51
B.2. Background samples	51

1. Introduction

The Large Hadron Collider (LHC), displayed as part of the CERN accelerator complex in Figure 3.1, and the ATLAS experiment, displayed in Figure 3.2, present an opportunity to find physics beyond the Standard Model (BSM) in the Higgs sector. Numerous BSM theories predict particles that could decay into two Higgs bosons. The search in the $HH \rightarrow bbWW^*$ channel is motivated by its high branching ratio and the possibility of a single lepton in the final state, which can be used as an additional handle in the reconstruction and analysis of the channel and to reduce the multijet background. The final state is composed of two b-jets, two light-quark jets from a hadronically decaying W boson, a lepton and a neutrino from the leptonically decaying W boson. For the investigation, events are simulated using pp collisions at $\sqrt{s} = 13$ TeV. Indications of such a BSM Higgs boson could be found by observing excesses in invariant mass distributions of m_{HH} . Reconstructing m_{HH} , or the complete event, of the 1-lepton final state of the $HH \rightarrow bbWW^*$ decay requires knowledge about the neutrino that comes from the leptonic decay of one W boson. A full event reconstruction is necessary to understand and measure the properties of the predicted particle. The momentum of the neutrino in the plane perpendicular to the beam axis can be inferred by determining the missing transverse momentum p_T^{miss} . The momentum along the beam axis, however, cannot be acquired with such an approach.

There are analytical approaches such as using the W boson mass constraint, but this method is insufficient for several reasons. The main reason for this is that there is always an off-shell W boson present that has a broad mass distribution and constraining it to a certain mass is not a good approximation. Using this constraint in combination with a constraint on the Higgs mass $m_{H \rightarrow WW^*}$ results in dropping a significant fraction of events due to requirements in the analytical solution.

This thesis presents an effort to estimate the neutrino's momentum along the z -axis, p'_z , in the single $HH \rightarrow bbWW^*$ channel utilizing neural networks. Neural networks have the potential to deliver good estimations for p'_z even with incomplete information. To that end, this thesis gives an overview of the workflow, performance and requirements that are expected when using neural networks for this analysis by presenting several approaches to

1. *Introduction*

training and evaluation. This approach is based on using 4-vector information of particles in the event to approximate p'_z .

2. Theoretical background

2.1. The Standard Model

The Standard Model (SM) is to date the best theoretical description of the elementary particles in our universe and their interactions. It describes twelve fermions, consisting of six quarks and six leptons, four gauge bosons and the Higgs boson [1]. The fundamental particles of the SM are displayed in Figure 2.1. The particles are grouped and differentiated by their distinct features. Such features include the spin, electrical charge, color charge, weak isospin and mass. The mass is used to categorize the fermions into three generations. The SM also is able to describe the electromagnetic (EM), weak and strong nuclear forces [2, 3]. Notably, gravity is not described by the SM.

The fermions in the SM are spin- $\frac{1}{2}$ particles. There are three charged leptons, the electron, muon and tau, which have an electrical charge of $-1e$ with e being the elementary charge. The electrically neutral leptons are the neutrinos which are named after their charged partners. The quarks are classified according to the flavors, the up-type and down-type quarks. The important quantity for this is the electric charge. With the down, strange and bottom quarks being down-type quarks they have an electrical charge of $-\frac{1}{3}e$. The up-type quarks, being the up, charm and top quarks have a charge of $+\frac{2}{3}e$.

One of the forces described by the SM is the weak nuclear force, which has two carrier particles. The weak nuclear force is described by the SU(2) gauge group. The W boson has a charge of $\pm e$ and the Z boson is electrically neutral. The weak force couples to the weak isospin T_3 of particles. This means it can only interact with particles that have $T_3 \neq 0$. Only fermions with a negative chirality or antifermions with a positive chirality possess a weak isospin. The W boson mediates between particles with $T_3 = +\frac{1}{2}$ and $T_3 = -\frac{1}{2}$, which promotes quark flavor and lepton flavor changes. The W boson therefore has an integer weak isospin of $T_3 = \pm 1$ depending on the direction of the transition. The W and Z bosons are the only massive gauge bosons. They are the third and fourth most massive particles in the SM with $m_W = 80.4 \text{ GeV}$ and $m_Z = 91.2 \text{ GeV}$. Their mass is acquired via the Higgs mechanism described in Section 2.1.1 [4].

The electromagnetic force is described in quantum electrodynamics (QED). The force

2. Theoretical background

carrying particle for QED is the photon. It is massless, it has no electrical charge and is a spin-1 particle. It couples to the electric charge of particles. The photon therefore does not self-interact. The symmetry of QED is built upon the U(1) gauge group.

The strong nuclear force is described by quantum chromodynamics (QCD) and is mediated by the gluon [5]. There are 8 gluons described within the SM but since the physics do not change for each of the gluons this is usually abbreviated by speaking of a single gluon. The gluon is massless, has no electric charge and, being a vector boson, it is a spin-1 particle. It couples to the color charge of particles. The color charge is carried by all quarks and the gluon itself, thus resulting in gluon self-interaction. There are three color charges, called red, green and blue. The three orthogonal charge states emerge from the SU(3) symmetry of QCD. Gluons and quarks are subject to color confinement, which states that particles with a color charge can only exist in colorless states. A combination of red, green and blue charges produces a colorless state. Further a color and an anticolor, which is carried by antiquarks, produce a colorless state. The states of multiple color charged quarks are called mesons in the case of one quark and one antiquark entering a state with colorless charge and baryons in the case of three quarks or antibaryons if three antiquarks are in a colorless state. For gluons the color confinement is expressed in short scale interactions, because gluons do not travel over macroscopic distances. If quarks in a colorless state are subjected to strong forces that drive them apart, the energy in the color field between the quarks is sufficient to pair produce new quarks. This results in the forming of new colorless states between the initial quarks and the newly formed quarks. This process ensures the confinement of the quarks. The ensemble of particles from this process usually propagate in the same direction within a narrow cone which is called a jet. Many particle analyses depend heavily on jets.

The forces of the SM can be differentiated also by their strength. The strength can be described in the form of the coupling constants α_i . These are not strictly constant though. The coupling constant of the EM force for example is "running" and changes with higher momentum transfers but the low energy value is $\alpha_{em} \approx \frac{1}{137}$. The other constants take values of $\alpha_{strong} \approx 1$ and $\alpha_{weak} \approx \frac{1}{30}$ but they are also running constants [6]. The strength of the weak interaction is suppressed because of the high masses of the gauge bosons.

It is important to note that many predictions of the SM are verified in experiments and measurements. The SM is the most successful description of particle physics to date. But it is evident that the SM is not a complete theory as there are multiple effects that cannot yet be explained by the SM, such as gravity and dark matter.

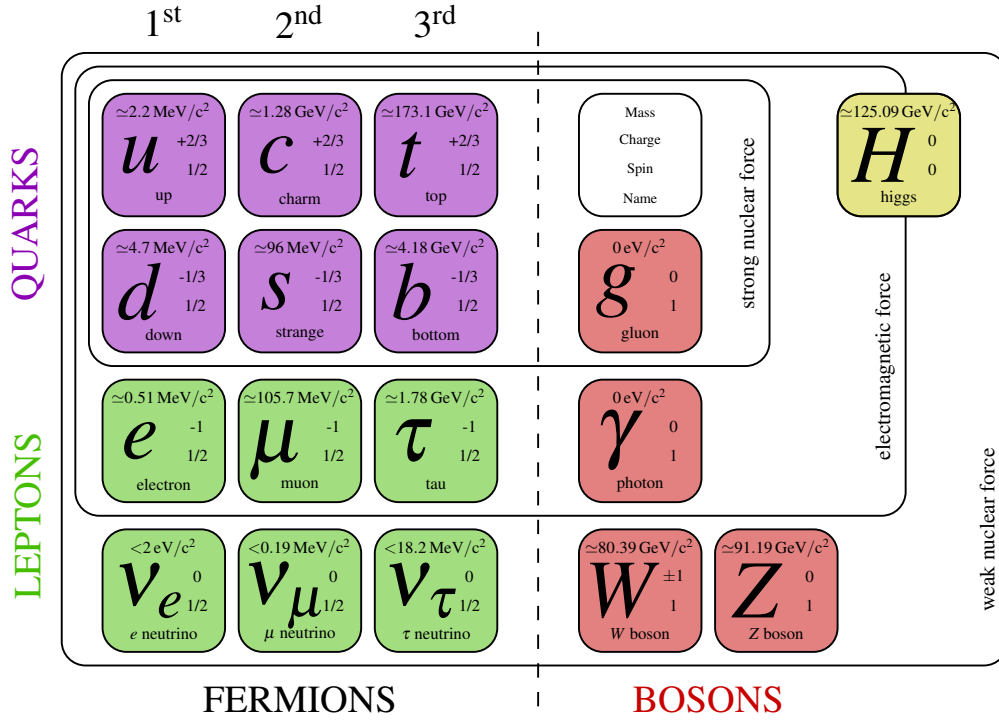


Figure 2.1.: The fundamental particles of the Standard Model. Diagram taken from Ref. [7]

2.1.1. The Higgs mechanism

The Higgs mechanism describes the breaking of the electroweak local gauge symmetry $SU(2)_L \times U(1)_Y$ [8]. The electroweak sector of the SM represents the unification of the weak nuclear force and the EM force. As already stated in Section 2.1, the Higgs mechanism gives rise to the masses of the W boson and the Z boson, as well as the fermions. Without the Higgs mechanism, these masses cannot be explained.

The Higgs mechanism involves two complex scalar fields in a weak isospin doublet

$$\phi = \begin{pmatrix} \phi^+ \\ \phi^0 \end{pmatrix} = \frac{1}{\sqrt{2}} \begin{pmatrix} \phi_1 + i\phi_2 \\ \phi_3 + i\phi_4 \end{pmatrix}. \quad (2.1)$$

The terms in the Lagrangian relevant for these fields are written

$$\mathcal{L} = (\partial_\mu \phi)^\dagger (\partial^\mu \phi) - V(\phi), \quad (2.2)$$

with the potential being referred to as Higgs potential

$$V(\phi) = \mu^2 \phi^\dagger \phi + \lambda (\phi^\dagger \phi)^2. \quad (2.3)$$

2. Theoretical background

The potential is required to have a finite minimum, called a vacuum state, therefore it is set to $\lambda > 0$. However μ can be chosen to be either $\mu^2 > 0$ or $\mu^2 < 0$. If $\mu^2 > 0$ is chosen the single vacuum state of the potential is at the origin and from that point the potential is symmetric in all directions. This changes when $\mu^2 < 0$ is chosen, because now the potential has acquired an infinite amount of vacuum states at a distance v from the origin. At the origin, the potential is not at the minimum. From the point of any of those vacuum states the potential is not symmetric anymore. The field can be expanded about such a minimum, which is chosen to be at

$$\langle \phi(x) \rangle_v = \begin{pmatrix} 0 \\ v \end{pmatrix} \quad (2.4)$$

without loss of generality and be written in unitary gauge yielding

$$\phi(x) = \frac{1}{\sqrt{2}} \begin{pmatrix} 0 \\ v + h(x) \end{pmatrix}. \quad (2.5)$$

The field $h(x)$ is identified as the physical Higgs field. In this representation the Lagrangian yields among other terms

$$\mathcal{L} \supset -\lambda v^2 h^2 - \lambda v h^3 - \frac{1}{4} \lambda h^4. \quad (2.6)$$

From the first term, which is quadratic in the Higgs field, we can infer the Higgs boson mass with $m_H = \sqrt{2\lambda}v$. The other terms give rise to the Higgs boson 3-point and 4-point self-interactions. The Higgs boson is therefore identified as the quantum excitation of this Higgs field. The resultant masses of the W and Z bosons are $m_W = \frac{1}{2}g_W v$ and $m_Z = \frac{g_W v}{2\cos\theta_W}$. The angle θ_W depicts the Weinberg angle, or weak mixing angle, [9] and is derived from the mass ratio of the W boson and the Z boson via

$$\sin^2 \theta_W = 1 - \left(\frac{m_W}{m_Z} \right) = 0.222\ 90(30) \quad (2.7)$$

$$\Rightarrow \theta_W \approx 28.17^\circ. \quad (2.8)$$

The mass of the fermions $m_f = \frac{1}{\sqrt{2}}g_f v$ is also dependent on the Yukawa coupling g_f , since one can construct gauge invariant mass terms from two Lagrangians. These Lagrangians are derived by a similar process as the W and Z boson masses. Though, one has to

account for the handedness of the fermions, thus obtaining:

$$\mathcal{L} = -g_f \left[\bar{L}\phi R + (\bar{L}\phi R)^\dagger \right] \quad (2.9)$$

$$\mathcal{L} = g_f \left[\bar{L}\phi_c R + (\bar{L}\phi_c R)^\dagger \right] \quad (2.10)$$

with L and R denoting left-handed and right-handed fermions and $\phi_c = -i\sigma_2\phi^*$. These Lagrangians also gives rise to a term that describes the interaction between the fermions and the Higgs boson.

2.1.2. The Higgs boson and Higgs boson pair production

The Higgs boson is subject of many analyses to date as it is the latest particle of the SM that has been discovered [10]. It was discovered in 2012 by ATLAS and CMS in the LHC at CERN. Next to precision measurements of the Higgs boson itself to pin down its properties, there are also efforts to use the Higgs boson in analyses involving BSM physics [11].

The Higgs boson is a spin-0 particle and the only scalar particle discovered thus far. The latest measurements of the Higgs boson suggest $m_H = 125.09$ GeV with a total cross section of $\sigma_H^{total} = 55.62$ pb at $\sqrt{s} = 13$ TeV for pp collisions [12]. The branching ratios (BR) of the Higgs boson as a function of m_H as predicted by the SM are displayed in Figure 2.2. The Higgs boson couples to itself, with the relevant Feynman vertices displayed in Figure 2.3. The measurement of this self-coupling strength is an important measurement for current physics [13].

It is possible to measure the self-coupling strength of the Higgs boson through Higgs pair production. The relevant leading order Feynman diagrams for this process are shown in Figure 2.4. In Figure 2.4(left) the off-shell Higgs boson is produced by gluon-gluon-Fusion (ggF) and a triangular loop of heavy quarks (bottom or top quarks). The quarks in the loop then couple via the Yukawa coupling to the virtual Higgs boson which then decays into two on-shell Higgs bosons with a coupling strength of λv , which allows for measurements of the Higgs self-coupling in this process. There are, however, also Higgs pair production processes that do not depend on the Higgs self-coupling and are therefore not suited for Higgs self-coupling strength measurements. A Feynman diagram for such a process is displayed in on the right of Figure 2.4. There the process only depends on the Yukawa coupling between the quarks in the loop and the Higgs bosons. The two productions both contribute to the *non-resonant* Higgs pair production but interfere destructively with each other. The SM predicts an inclusive ggF HH cross section of

2. Theoretical background

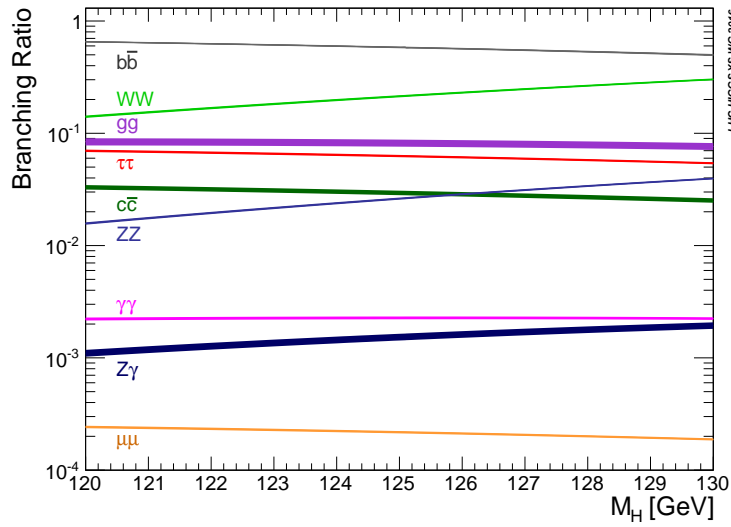


Figure 2.2.: SM Higgs boson decay BRs as a function of m_H . Current measurements suggest $m_H = 125.09$ GeV [14].



Figure 2.3.: Feynman diagrams of the Higgs boson self interactions and the respective couplings strengths.

$\sigma_{HH}^{ggF} = 31.02$ pb assuming $\sqrt{s} = 13$ TeV in pp collisions and $m_H = 125.09$ GeV [12]. Other Higgs pair production modes have significantly lower cross sections.

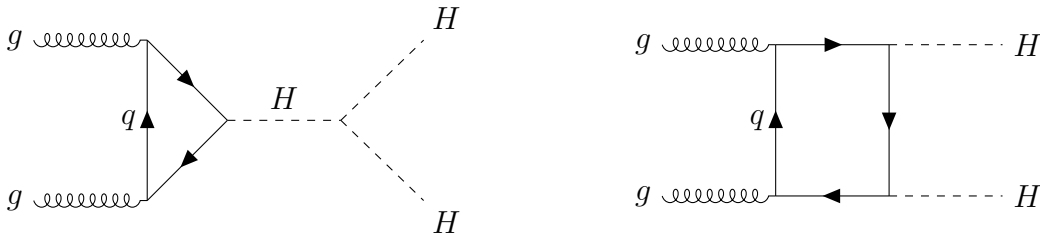


Figure 2.4.: Leading order Feynman diagrams for Higgs pair production at the LHC with a triangular loop and Higgs self-coupling (left) and with a box loop (right).

The search for Higgs pair production is also motivated because several BSM theories predict, among others, heavy particles that are expected to decay into two SM Higgs

bosons. A selection of such BSM theories is more closely discussed in Section 2.2. A candidate process that would include the production of a BSM Higgs boson which decays into a pair of Higgs bosons is the process of the Feynman diagram shown in Figure 2.5. In this diagram, the aforementioned off-shell Higgs boson H is replaced with a heavy on-shell BSM particle X . This production mode is called *resonant* Higgs pair production.

The search for resonant Higgs pair production would benefit greatly from the reconstruction of the resonant HH mass. The data mentioned in the following thesis stems exclusively from the simulation of pp collisions at $\sqrt{s} = 13$ TeV. The decay mode used in this thesis is the $HH \rightarrow bbWW^*$ decay with one leptonically decaying W boson. This reconstruction requires the measured kinematic information of objects in the final state. These objects include two b-jets, two light quark jets and a lepton (leptons refers to either a muon or an electron). From the jets the reconstruction of $m_{H \rightarrow bb}$ and $m_{W_{\text{had}}}$ is possible. For $m_{W_{\text{lep}}}$ and therefore $m_{H \rightarrow WW^*}$, however, the kinematic information of the neutrino, that is associated with the W_{lep} decay, is necessary.

The neutrino's energy and momentum cannot be measured directly but the energy and momentum in the transverse plane can be acquired by measuring E_T^{miss} . The p_z' component cannot be obtained by measurements or be calculated exactly with analytical methods. The mass of the di-Higgs system m_{HH} is not highly dependent on the kinematics of the neutrinos as the neutrino carries only small amounts of kinetic energy compared to other particles in the final state. But m_{HH} is still affected by the missing p_z' and its uncertainties. The possible gains in performance of the m_{HH} and the possibility to reconstruct $m_{H \rightarrow WW^*}$ are the motivation of this thesis' efforts to acquire an approximation for p_z' with neural networks.

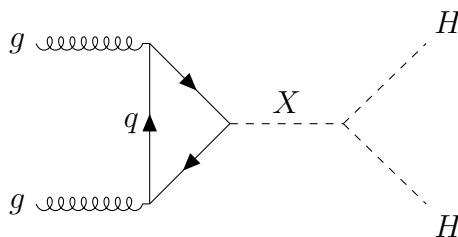


Figure 2.5.: Feynman diagram for resonant Higgs pair production at the LHC with a triangular loop and a BSM particle X .

2.2. Extensions of the Standard Model

There are several attempts to extend the SM in order to find possible explanations for phenomena that currently cannot be explained by the SM. However, these models beyond the SM must also be consistent with the measurements already made.

One such class of models would be the two Higgs doublet model (2HDM) [15]. In addition to the already existing complex Higgs doublet in the SM, a second complex Higgs doublet is introduced. The two complex Higgs doublets also result, amongst others, in the existence of five physical scalar states, i.e. five Higgs bosons. Two Higgs bosons, H and X , are CP even and electrically neutral in terms of electric charge. The X boson is heavier than H boson per construction. In the alignment limit, the light H boson would have couplings that are similar to those of the SM Higgs boson. The X boson could be a potential candidate for the heavy resonance of the simulated data investigated in this thesis. The other Higgs bosons are a electrically neutral CP odd pseudoscalar A and two charged Higgs bosons H^\pm . Testing the 2HDM by observing the SM Higgs boson is crucial to make a more compelling argument for or against 2HDM.

A motivation for the 2HDM model is to potentially give rise to the required number of Higgs bosons for super-symmetry (SUSY) [16]. Two Higgs doublets are a structural requirement to suppress anomalies that would otherwise arise for SUSY. Next to the additional Higgs boson SUSY introduces *super-partners* for all particles of the SM. It is a sensible assumption that the SUSY particles have a mass scale of at least $\mathcal{O}(\text{TeV})$, since lower masses have been excluded by experiments.

The search for evidence or proof of BSM physics is one of the main goals of current physics.

3. The Large Hadron Collider and the ATLAS experiment

3.1. The CERN accelerator complex

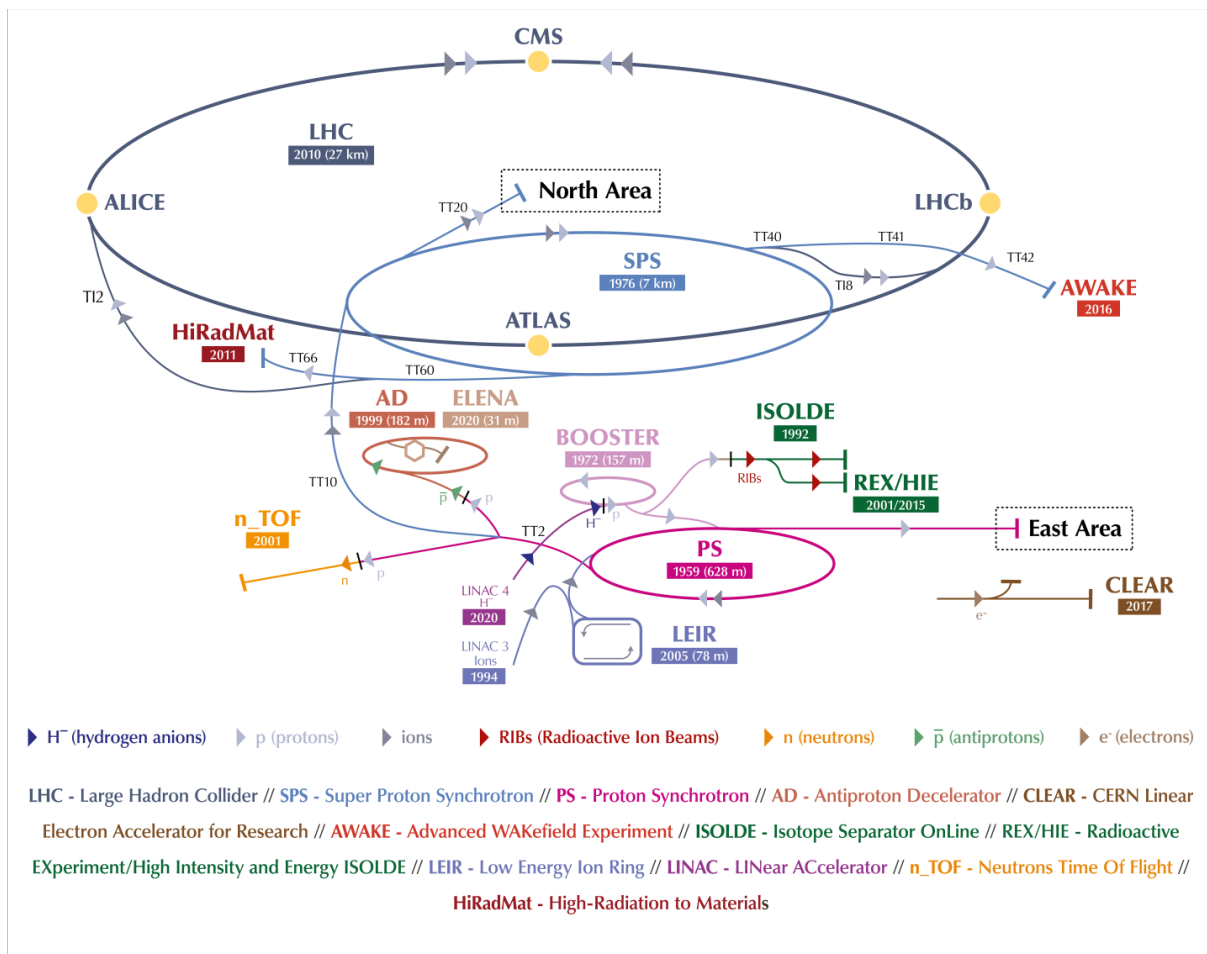


Figure 3.1.: Diagram of the CERN accelerator complex [17].

3. The Large Hadron Collider and the ATLAS experiment

The CERN accelerator complex is comprised of multiple synchrotrons, linear accelerators and other experiments. The CERN accelerator complex is displayed in Figure 3.1. At CERN there are accelerators for protons, antiprotons, heavy ions and electrons. The biggest accelerator at CERN to date is the Large Hadron Collider (LHC), a synchrotron with a circumference of close to 27 km. It is built 175 m below the surface to shield it from outside radiation but also keep outgoing radiation contained as most of the radiation is emitted in the plane of the accelerator. The LHC is a proton-proton collider.

Smaller and older experiments that are partly superseded by the LHC are used as boosters to bring the protons to the minimum velocity for the LHC to use them. First, protons are accelerated in the linear particle accelerator LINAC 2 bringing them to an energy of 50 MeV. In the Proton Synchrotron Booster (PSB), protons are brought to an energy of 1.4 GeV. The Proton Synchrotron (PS) then accelerates the protons up to 26 GeV and the Super Proton Synchrotron (SPS) to 450 GeV, at which point the protons are injected into the LHC.

There are four experiments at the LHC, ALICE, LHCb, CMS and ATLAS. With ATLAS and CMS being general purpose experiments, they do not specialize in detecting certain types of particles but concentrate on measurements of a multitude of processes. The ALICE experiment is a heavy ion collider experiment and is exploring key issues in QCD like quark deconfinement and quark-gluon plasma. The LHCb experiment concentrates on b-physics and primarily measures CP violation.

The LHC provides bunch crossings at a rate of 40 MHz with up to 10^{11} protons per bunch. This results in a peak design luminosity of $10 \times 10^{34} \text{ cm}^{-2}\text{s}^{-1}$. The LHC has operated at multiple energies over time. In Run 1 the LHC operated at a center-of-mass energy of $\sqrt{s} = 7 \text{ TeV}$ producing 5.46 fb^{-1} of data from 2010 to 2011 and at $\sqrt{s} = 8 \text{ TeV}$ producing 22.8 fb^{-1} of data from in 2012. After 2012 the LHC was taken offline to prepare Run 2 beginning in 2015, where the LHC operated at $\sqrt{s} = 13 \text{ TeV}$. Run 2 produced 139 fb^{-1} of data from 2015 until 2018. In 2018 the LHC was shut down again to prepare Run 3.

3.2. The ATLAS experiment

The ATLAS experiment [18] is a general purpose detector with a cylindrical and forward-backward symmetry with respect to the interaction point, where the proton-proton (pp) beams collide. The detectors dimensions are 25 m in height and 46 m in length, and the detector weighs 7 Gg. The ATLAS experiment uses a right-handed coordinate system with the beam axis being defined as the z -axis and the xy -plane is transverse to the beam

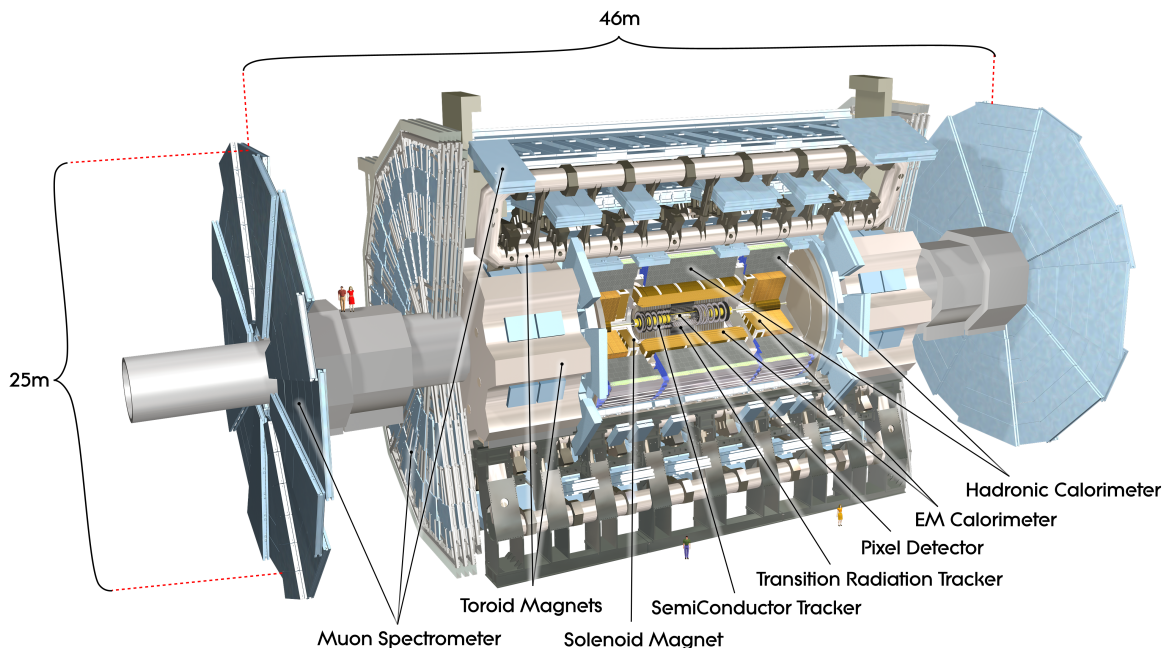


Figure 3.2.: Cut-away view of the ATLAS detector [18].

direction. The positive x -axis points from the interaction point to the center of the LHC and the positive y -axis points upwards. The detector is comprised of multiple detector subsystems. These are arranged concentrically with increasing radius as the detectors are layered upon each other, or as layered end-caps of the cylinder and closing off its sides. A cut-away view of the ATLAS experiment is displayed in Figure 3.2. The end-caps account for particles with high pseudo-rapidity values, $\eta \equiv -\ln \left[\tan \frac{\theta}{2} \right]$, where θ , the polar angle, is the angle between the measured object and the positive direction of the z -axis. The angle ϕ describes the azimuthal angle. The pseudorapidity η converges for particle velocities close to the speed of light towards the rapidity $y = \frac{1}{2} \ln \left[\frac{E+p_z}{E-p_z} \right]$. For massless particles, η and y are equal. The difference between two pseudorapidity values is approximately invariant for Lorentz boosts along the beam axis. The ATLAS experiment has almost full azimuthal coverage apart from technical necessities like the standing feet of the apparatus. The maximum polar coverage is at $|\eta| = 4.9$ for EM and hadronic energy measurements in the end-caps.

The ATLAS experiment has four major detector systems, the inner detector (ID), the electromagnetic calorimeter (ECAL), the hadronic calorimeter (HCAL) and the muon spectrometer.

The innermost detector is the ID. It is made up of silicon semiconductor pixels and strips

3. The Large Hadron Collider and the ATLAS experiment

and the transition radiation tracker (TRT) at its outer perimeter. The TRT is made up from gaseous straw tubes filled with a mixture of Xe/CO₂/O₂ gases. The objective being a measurement of momentum and charge of electrically charged particles without impeding the momentum of the particles. The ID provides momentum measurements and primary, as well as secondary, vertex measurements for charged tracks with $|\eta| < 2.5$. Furthermore it contributes to electron identification within $|\eta| < 2.0$ in addition to the electromagnetic calorimeter. The electrons are identified when transition radiation is emitted by highly relativistic electrons. The transition radiation is EM radiation that is emitted when charged particles move through an inhomogeneous medium and happens at polymer fibers between the straw tubes. The ID operates inside a magnetic field generated by a solenoid with a field strength of 2 T. As this detector is closest to the high energy particle collisions, it is exposed to the most radiation. To counteract the resulting radiation damages to the silicon sensors, the ID is cooled to about -5°C to -10°C . The resolution of the ID for the transverse momentum of charged tracks is $\frac{\sigma_{p_T}}{p_T} = 0.05\% p_T \oplus 1\% [\text{GeV}]$.

The next detector subsystem is the calorimeter system. It is made up of one barrel region in shape of a cylinder around the beam axis and two end-caps. The calorimeter consists of two alternating materials. The first layer is the absorber material and the second layer, or active layer, is the sampling material. Used absorber materials in the different calorimeter sections are steel, lead and tungsten. The active layers use liquid Argon or scintillating tiles. The absorber layer causes particles to shower in the calorimeter and in the sampling layer, the energy deposits are measured. The calorimeter is divided into two sections each detecting different particles. The ECAL specializes in detecting particles that interact via the EM force. The HCAL specializes in detecting particles that interact via the strong nuclear force. Although the calorimeters are specialized towards certain interactions, in practice there is no clean cut between the two calorimeters and what particles they measure. The calorimeter section is situated between the inner solenoid magnet and the outer toroidal magnetic field.

The first, and inner, calorimeter is the ECAL. It mainly measures the energy of photons and electrons as they pass through the detector material. Here, the electrons and photons shower and are absorbed by the detector after passing through multiple radiation lengths worth of matter. The physical processes the showering is based on, are pair productions of electrons and positrons and bremsstrahlung. Both processes are reliant on the presence of matter. The nominal energy resolution of the ECAL for EM showers is $\frac{\sigma_E}{E} = 10\%/\sqrt{E} \oplus 0.7\% [\text{GeV}]$.

The second calorimeter layer is the HCAL. It measures hadrons in similar fashion as the EM calorimeter does. The hadrons shower and are absorbed by the calorimeter

material. Hadronic showers are the result of strong interactions between the hadrons and the detector material resulting in the production of other hadrons. Usually there are also EM showers accompanying hadronic showers. Its energy resolution for hadronic showers are $\frac{\sigma_E}{E} = 50\%/\sqrt{E} \oplus 3\%$ [GeV] for the barrel and end cap region and $\frac{\sigma_E}{E} = 100\%/\sqrt{E} \oplus 10\%$ [GeV] for the forward region.

The calorimeters allow for measurements between $0 < |\eta| < 3.2$ with additional hadronic calorimeter coverage at pseudo-rapidities of $3.1 < |\eta| < 4.9$ for the forward region of the calorimeter.

The outermost detector is the muon spectrometer. It is designed to detect the charged particles, predominantly muons, that are not stopped by the calorimeters in the barrel, as well as the end-cap region. The muon spectrometer relies on gas-filled drift chambers. When a muon travels through the chamber it ionizes the gas inside. This causes a cascade of ionization and the built up charge is measured with wires throughout the chamber. The muon spectrometer is capable of measuring the particles momenta within $|\eta| < 2.7$ and capable on triggering on charged particles within $|\eta| < 2.4$. This is achieved by three layers of detectors in the form of three concentric shells in the barrel region and four end-caps at each side. Each shell in the barrel region has overlapping detector chambers as reference for relative alignment measurements of the detector parts. The tracking performed by the muon spectrometer works complementary to the tracking performed by the ID. A total of three toroid magnets with 8 coils each are deployed within the muon spectrometer with one toroid magnet placed along the beam axis as barrel toroid and one toroid magnet placed on each end-cap. These toroids produce a bending power of $1\text{ T} \cdot \text{m}$ to $7.5\text{ T} \cdot \text{m}$ and achieve a peak magnetic field strength of 3.9 T to 4.1 T in the windings of the barrel and the end-cap toroid respectively. The individual detector chambers are made up of four different types of drift chambers, each having its strengths and weaknesses, depending on their task and position in the detector. The muon spectrometer achieves a momentum resolution of $\frac{\sigma_{p_T}}{p_T} = 10\%p_T$ [GeV] at $p_T = 1\text{ TeV}$.

ATLAS uses a trigger system to record the collision data. The ATLAS Level 1 trigger is hardware-based and responsible to quickly decide which information of the huge amounts of data that is produced by all the different detectors is kept. It does this by identifying the incoming data with particles and objects like hadronic jets. This is based upon predefined criteria. These criteria usually identify hard-scatter events with high energy particles in which we are interested as oppose to soft-scatter events with low energy particles. It decides to discard events within a latency of $2.5 \times 10^{-6}\text{ s}$. This event selection is also necessary reduce the data load for the high level trigger (HLT) from 40 MHz to 100 kHz. It also marks Regions-of-Interest where it detects special patterns and features

3. The Large Hadron Collider and the ATLAS experiment

for reconstructions of the HLT. The HLT is software based and performs full or partial event reconstruction from information passed on by the Level 1 trigger. The HLT passes on interesting events upon predefined criteria at a rate of 1.5 kHz to the subsequent data collection where the events are saved to hard drives in the data storage and reconstructed for analysis.

4. Neural networks

4.1. The theory of neural networks

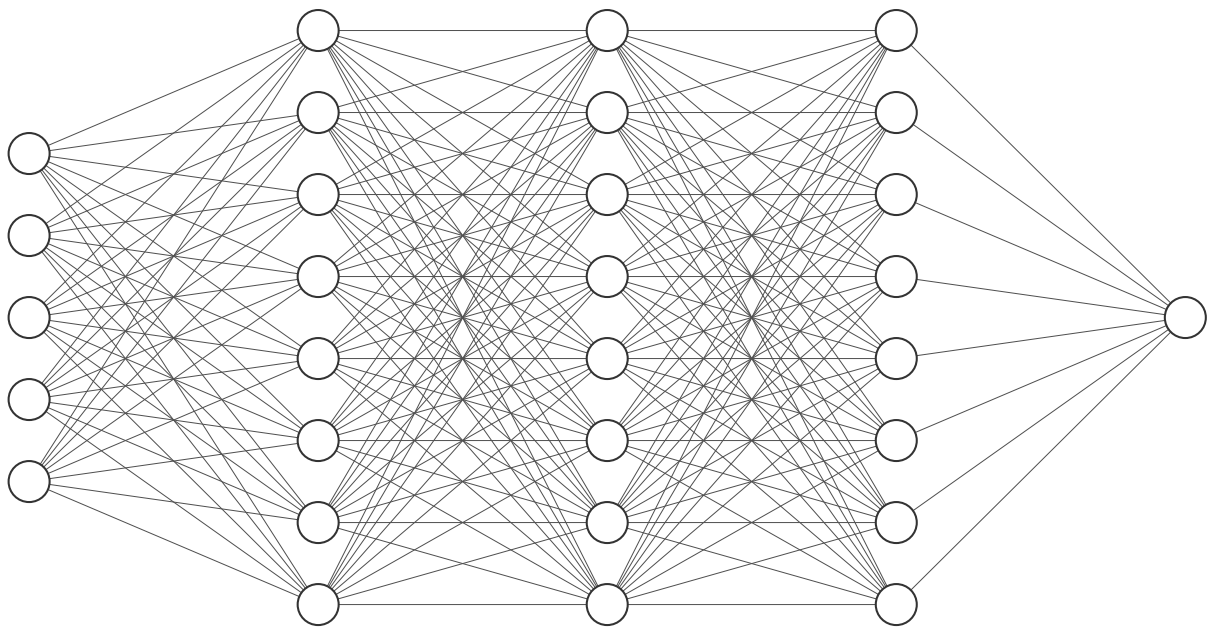


Figure 4.1.: Schematic of a neural network with five inputs, one output, three hidden layers and eight neurons per hidden layer.

The goal of a neural network (NN) is to map a set of correlated variables that stem from measurements or simulations to a set of outputs. This function can be described as a cost function and is being minimized by the NN during the training. An NN consists of layers of neurons, where neurons resemble an intermediate step in the calculation of the cost function. The first layer of neurons takes on the input variables as values. A schematic of a NN is displayed in Figure 4.1. The a^{th} neuron in a following layer i receives the preceding value of the b^{th} neuron of the $(i - 1)$ th layer as $x_i^a = f_i(w_i^{ab}x_{i-1}^b + b_i^a)$, where w_i^{ab} is the weight that connects the two neurons, b_i is the bias and f_i is the activation function for the i^{th} layer. The activation function is a non-linear function that acts like a converter and is inspired by biological neurons. Biological neurons can either fire or not fire but they cannot fire negatively. This behavior can be simulated by implemented

4. Neural networks

a Heaviside step function or a rectified linear unit (ReLU). The bias acts as a constant with which the activation function can be shifted. This thesis solely used ReLU with $f(x) = \max(0, x)$ as an activation function. The weight and the bias are subject of the training and are initialized with some values. All neurons of a layer are connected to all neurons of adjacent neurons but there are no weights that connect neurons across non-adjacent layers. The introduced cost function describes all these individual links between the neurons. To minimize this cost function will be the objective of the training. The numbers of neurons, hidden layers, input and output variables can be chosen arbitrarily but these values have to be defined before the training and cannot be changed during the training. The layers between the input and the output layer are called hidden layers and when there is more than one hidden layer the NN is called a deep NN.

The sets of input variables are then fed into the NN and an output is generated. The output is then compared to a reference and the mean squared error (MSE) between them is calculated. The cost function of the MSE is then gradually minimized by taking a step towards a local minimum using gradient descent. With each step taken the weights between the neurons are changed according to the present position. Around the local minimum one can define a dropout interval, the minimum delta. When crossing the dropout interval a number of times, defined in patience, the training is concluded and the optimized function is set. This method of concluding the training before reaching the defined number of epochs is called *early stopping*. Now the function can be used on orthogonal data to produce an output according to the found correlations in the training. This step is called evaluation of the NN.

4.2. Application of the neural network

The subject of this work is to obtain a sensible approximation for the missing p_z' to achieve a full event reconstruction in the $HH \rightarrow bbWW^*$ channel in the 1-lepton final state. The process is displayed in Figure 4.2. The input variables consist of the 4-vector components of three other particles in the event, namely the lepton of the leptonically decaying W boson (W_{lep}), the Higgs boson of the $H \rightarrow bb$ decay and the hadronically decaying W boson (W_{had}), and the p_x^{miss} , p_y^{miss} of the associated event. This yields a total of 15 variables. The truth as well as reconstructed variables are available but the final NN should only use reconstructed variables. A training on truth variables and on reconstructed variables are called truth training and reco training respectively. The training data stems from MC simulation because access is needed to the truth p_z' for the training process as the experience. The evaluation also happens on simulated data but can in principle also be

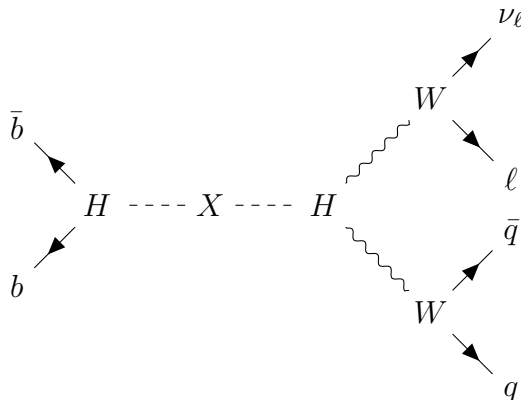


Figure 4.2.: Feynman diagram of the $HH \rightarrow bbWW^*$ channel. Depending on the charge of the W bosons either the lepton or the neutrino is an antiparticle.

executed on measured data. The advantage for an evaluation on simulated data is that the truth p_z^ν is still present and can be used to compare the output. The samples used to simulate the signal events are listed in Appendix B.1.

The dataset for each mass point is split into three parts, the training, the validation and the evaluation samples. The training sample contains 20% of the events and the validation sample contains 40%. Both are used for the training algorithm. The training set is used for the training itself while the validation set is used to monitor the NN at any stage to detect and reduce overfitting. This happens by evaluating the NN during the training and measuring the MSE between the output and the truth p_z^ν . If the MSE increases due to overfitting the course of the NN training will be changed accordingly. The evaluation sample contains 40% and is used in the evaluation algorithm on the NN after finishing the training.

Next to the input variables, one has to provide the hyperparameters for the NN. In this analysis the following hyperparameters have been used:

- Number of neurons: The number of neurons defines how many neurons are present in a hidden layer. The number of neurons per hidden layer can vary for each hidden layer.
- Number of hidden layers: The hidden layers are the layers of neurons which are between the input layer and the output layer.
- Number of epochs: The number of epochs defines how often the NN training algorithm runs over the entire training set.

4. Neural networks

- Batch size: The batch size of the chunks of training data the NN processes before updating the model.
- Minimum delta: The minimum delta is a positive value and is used for *early stopping*. If the absolute change of the MSE is smaller than the minimum delta the change does not qualify as improvement.
- Patience: If the number of epochs that did not yield an improvement is equal to the patience, the training is stopped.
- Activation: The activation defines the activation function with which the neurons value is determined in the hidden layers. The activation functions are chosen from a set of available options.
- Last activation: The last activation defines the activation function for the output layer.
- Learning rate: Describes the how much a model changes in response to the measured error

These hyperparameters describe how the training is executed and represent its settings, like the aforementioned number of neurons and hidden layers. The hyperparameters can be changed and will be changed during the course of the analysis but have to be set before every training. Different input sizes, that is number of variables and/or number of events, different types of outputs and different optimizers perform best with suiting hyperparameters. A table of the used hyperparameters and optimizers can be seen in Table 4.1. The starting hyperparameter set will also be called Set 1 and the final set of hyperparameters Set 2 for the remainder of this chapter. There are also optimizer specific variables that can be configured. For SGD two additional variables have been considered. The decay rate determines the impact of data on the training over time. A positive decay rate results in a decrease of the learning rate for each time step. The momentum prevents oscillations and potentially results in faster convergence of the SGD method by building up velocity.

Hyperparameters	starting parameters	final parameters
Neurons	60	40
Hidden layers	4	3
Epochs	100	40
Batch size	32	64
Minimum delta	-	-
Patience	-	-
Dropout rate	0.0	0.0
Activation	ReLU	ReLU
Last activation	linear	linear
Optimizer	starting parameters	final parameters
Type	SGD	SGD
Learning rate	0.01	0.0001
Momentum	0.0	0.99
Decay rate	0.0	0.0

Table 4.1.: List of the neural networks hyperparameters for its starting point and its final version. The parameters that are particularly connected to the optimizer are displayed separately in the lower half.

5. Analysis

5.1. Measures

To evaluate the performance of the NN and its subsequent output, several measures have been introduced, which all compare the NN output against a reference. The raw output, the estimate of the p'_z , called NN p'_z in the following, can be compared to the p'_z of the simulated neutrino on truth level, the true p'_z . Further, the p'_z can be used to build invariant masses of particles preceding the neutrino in the decay chain, such as $m_{H \rightarrow WW^*}$ and m_{HH} . Now, there are several options how to reconstruct such a mass. It can be built from either reconstructed variables, truth variables or a mixture of those and the true p'_z or NN p'_z , respectively. However, the reference always uses the true p'_z , the NN output always uses the NN p'_z . Comparing the invariant masses allows insight into the effects of an inaccurate p'_z estimate on the invariant mass distributions.

In addition to a visual comparison of distributions, a discrete measure to easily quantify the differences is introduced. The difference between distributions is measured in terms of the width of response distributions $\frac{\text{Value containing NN } p'_z}{\text{Value containing true } p'_z}$. The values for the response distribution can be either p'_z itself or an invariant mass built from p'_z . The width is defined as the 1σ range in which 68% of the entries are situated, centered around the median. With this measure, the response of p'_z or an invariant mass can be expressed by a single number summarizing the results.

This method, however, also has some limitations. For one, the measure cannot differentiate for different compared distributions. Thus, two comparisons of invariant masses against the same reference could be assigned a similar 1σ range, although the tested distributions that contain the NN p'_z exhibit very different behavior. One such example would be that one training produces an output that shifts the mass peak but retains the overall width and structure of the mass distribution compared to the shape of the reference distribution. The other training could produce an output that broadens the shape of the mass distributions in a way that the peak is exactly at the same value but almost vanishes as a result of the broadening. There is no single variable or measure to quantify such different behavior without examining the distributions themselves. Another problem

5. Analysis

that arises is not limited to the width of response distributions but also affects the mass and p'_z distributions themselves. There is no way to know if the NN took into account the proper dependencies and correlations or if the training essentially failed but the output of the NN looks similar to the reference. This can only be ruled out by looking at a sufficient number of evaluations of the NN with sufficiently large datasets.

5.2. Single mass point training

The first NN training performed is a simple training on events of one mass point and evaluated on events of the same mass point. This matching of mass points for training and evaluation will also be called a native training and evaluation. The training is performed with the hyperparameter set 1 from Table 4.1 and the input variables used are the standard set of 15 variables displayed in Table 5.1. The training is conducted on truth variables since this study is supposed to validate the basic concept of the NN. The training on truth variables is presumed to have an improved performance over the training on reconstructed variables as the NN does not have to take the resolution and uncertainties of the reconstructed variables into account. A separate training under the same conditions but on reconstructed variables is conducted to compare the performances and assess the impact of the reconstruction in the training. The distributions of the NN p'_z compared to the truth p'_z can be seen in Figure 5.1. The responses are displayed in Appendix A.1. One can clearly see the difference between the trainings in the p'_z distributions. In Figure 5.2, it is also visible how the p'_z performance differences carry through to the invariant masses $m_{H \rightarrow WW^*}$ and m_{HH} , although they are not as pronounced as in the p'_z distributions. Looking at the truth variable training one can also find that the NN has the ability to provide a very good approximation of the p'_z , even without tweaking the hyperparameters or using elaborate methods and inputs.

4-vector	$H \rightarrow bb$	W_{had}	Lepton	MET
p_x	$p_x^{H \rightarrow bb}$	$p_x^{W_{\text{had}}}$	p_x^{lep}	p_x^{miss}
p_y	$p_y^{H \rightarrow bb}$	$p_y^{W_{\text{had}}}$	p_y^{lep}	p_y^{miss}
p_z	$p_z^{H \rightarrow bb}$	$p_z^{W_{\text{had}}}$	p_x^{lep}	-
E	$E^{H \rightarrow bb}$	$E^{W_{\text{had}}}$	p_x^{lep}	E_T^{miss}

Table 5.1.: List of the used standard set of 15 input variables for the NN.

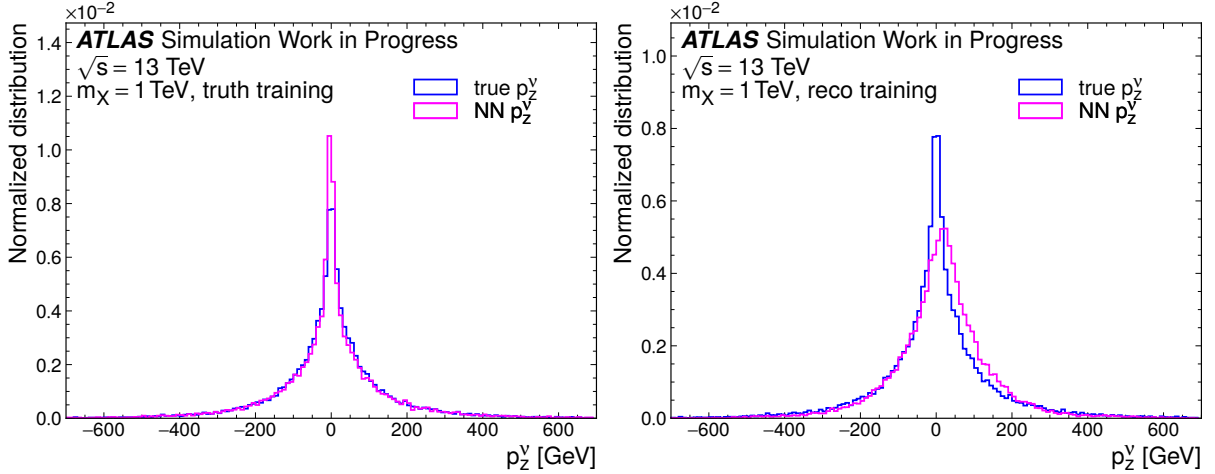


Figure 5.1.: Distributions of the NN p_z^v compared to the truth p_z^v . The NN is trained on truth variables (left) and reconstructed variables (right).

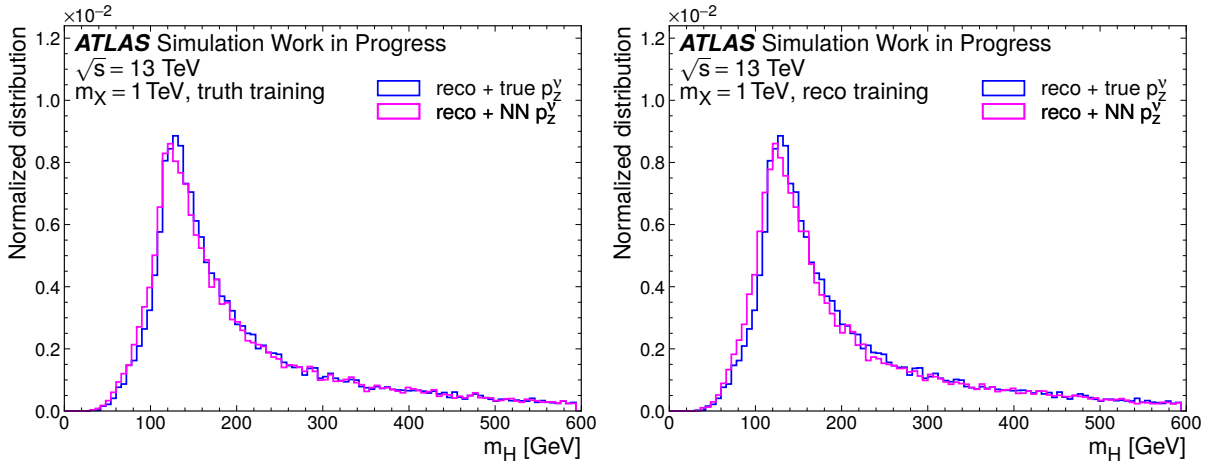


Figure 5.2.: Distributions of m_H calculated from reconstructed variables and NN p_z^v compared to m_H calculated from reconstructed variables and truth p_z^v . The NN is trained on truth variables (left) and reconstructed variables (right).

5.3. Training on multiple mass points

With the training method in Section 5.2, it is necessary to train one NN for every mass point. This section describes an effort to reduce the number of NNs needed for the analysis by retaining the number of mass points covered by the analysis. The basic concept being to train a NN on a combination of events of multiple mass points. This NN is then supposed to cover multiple mass points for the analysis.

This method entails to evaluate the NN with a set of events that is possibly very different from the training and validation sets both in terms of the number of events and magnitude

5. Analysis

of the kinematic variables. The energies of the decay particles are usually significantly lower for a resonance with $m_X = 0.8$ TeV than for a resonance with $m_X = 5$ TeV. The effect of training and evaluation sets of different mass points are assessed for single mass point trainings before training on groups of mass points. To do this, three mass points across the range of mass points are chosen for NN trainings to roughly represent low, medium and high mass points: $m_X = 1.2$ TeV, $m_X = 2$ TeV and $m_X = 4$ TeV. The resulting NNs are then evaluated on all available evaluation sets of single mass points. The performances of the three NNs are compared to the performances of native pairings for each mass point.

The widths of the response distributions of m_H are displayed in Figure 5.3. The distributions for $m_X = 1$ TeV and $m_X = 3$ TeV are displayed in Appendix A.2. Two tendencies can be inferred from the results. Firstly, the width of the native test series increases for higher mass points. This is probably the result of the low statistics for the high mass point events. Secondly, the width for the non-native pairings of training and evaluation sets increases significantly the bigger the difference in mass for the two sets is.

In the next step, NNs are trained on sets of multiple mass points. The mass point groups contain three to twelve mass points. A training on twelve mass points is equal to a training on all the available simulated events in this study.

The widths of the response distributions of m_H for a selection of mass point groups are displayed in Figure 5.4. The distributions for $m_X = 1$ TeV and $m_X = 3$ TeV are displayed in Appendix A.3. One can see that the overall behavior of the NN does not change from the single mass point trainings in Figure 5.3. The native pairings used as reference in both figures are equal. The two identified tendencies are still present. The width generally increases towards higher mass points and the width increases significantly when the mass point of the evaluation is not part of the group of mass points the NN is trained on. The latter tendency, however, can be avoided by the NN that is trained on all mass points. Also the NN trained on mass points between $m_X = 0.9$ TeV and $m_X = 4$ TeV covers enough mass points and is close enough to the two mass points which are not included in the training that this effect can be mitigated. The low statistics, also “low stat”, group is a control group to assess the impact of the higher statistics present in the sets of multiple mass points. The statistics were cut individually for every mass point to match the statistics of the native pairing. Therefore we can see the positive impact of higher statistics on the performance as the difference between the $m_X = 0.9$ TeV to $m_X = 4$ TeV NN and the $m_X = 0.9$ TeV to $m_X = 4$ TeV low stat NN. The loss in performance introduced by generalizing the NN can be seen as the difference between the widths of the native pairings and the $m_X = 0.9$ TeV to $m_X = 4$ TeV low stat NN.

The consequence taken from this investigation is that it is sufficient and even beneficial for some mass points to only use a single NN trained on all mass points in terms of performance. This also simplifies the application of such a NN in the analysis workflow.

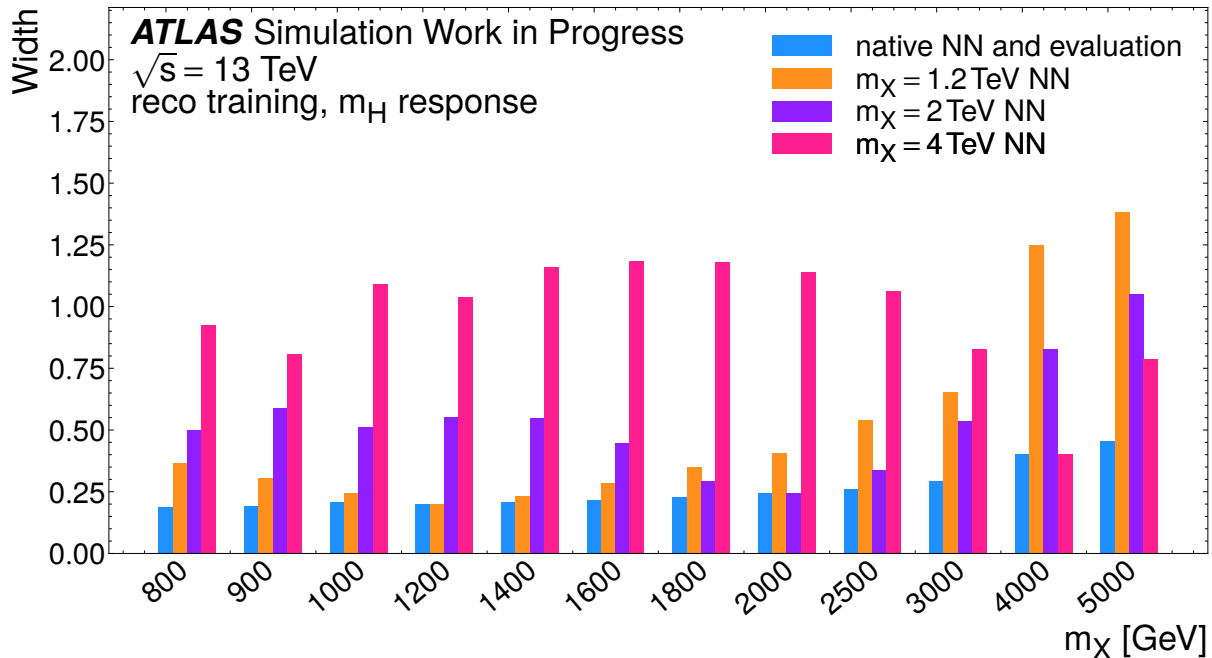


Figure 5.3.: 1σ ranges for m_H calculated from reconstructed variables and NN p'_z versus m_H calculated from reconstructed variables and truth p'_z . Training is on reconstructed variables and for varying mass points.

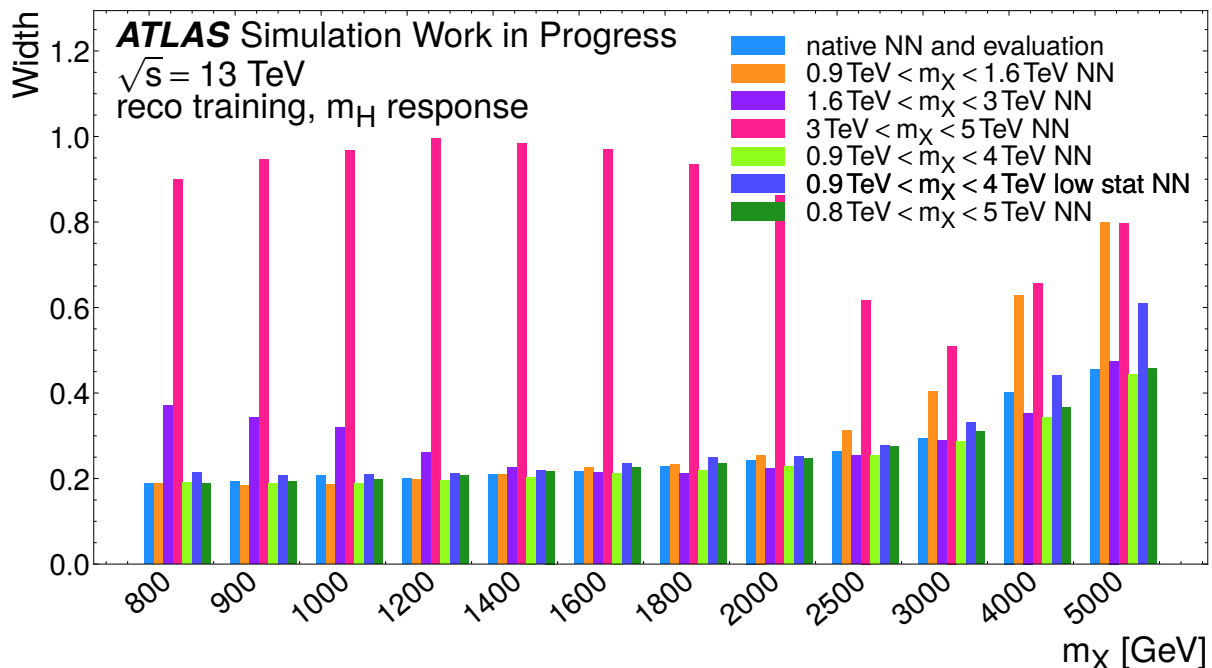


Figure 5.4.: 1σ ranges for m_H calculated from reconstructed variables and NN p_z^ν versus m_H calculated from reconstructed variables and truth p_z^ν . Training is on reconstructed variables and on varying mass point combinations.

5.4. Input variables

To understand the role of the individual variables better the input variables are changed to exclude the four components of one of the 4-vectors. Subsequently the created training sets include only eleven input variables and in the case of training without the MET 4-vector components there are twelve input variables. The training and evaluation are kept on one the same mass point to isolate possible effects of this training. The distributions of p_z^ν and m_H can be seen in Figure 5.5 and the 1σ ranges in Figure 5.6 for $m_X = 2$ TeV. This investigation produces three interesting findings.

The first finding is that the NN is very resilient towards missing variables as the performance is hardly impacted by reducing the number of input variables significantly such that a training without the $H \rightarrow b\bar{b}$ 4-vector and the lepton 4-vector is almost identical to a training on the full set of reconstructed variables. This opens the possibility of cutting out individual variables if their measuring precision is too low or a variable is difficult or outright impossible to measure. If the performance is affected, as it is the case for the missing W_{had} or MET 4-vector the performance does not suffer too harshly. In such an event, one could probably still justify not using certain variables if they are poorly modelled.

Secondly the training without $H \rightarrow b\bar{b}$ 4-vector even decreased the 1σ range. Even though the actual difference is minimal it demonstrates the possibility of gaining precision for the NN. In the present case, however, the performance gain seems to be too small to pick up this lead.

The third piece of information is also an insight into how the NN works. The dependency of the different 4-vectors towards the p_z^ν does not seem intuitive, as one would believe that the lepton and MET variables are most important for the reconstruction of our discriminating variable. Accordingly, the W_{had} and the $H \rightarrow b\bar{b}$ should have a lower impact. But the situation depicted in the 1σ ranges does not reflect this exact picture. The important take away would then be that we cannot necessarily apply intuition to the NNs results. Though, one could consider to influence the NNs decision making on the importance on variables by applying some kind of weighting to variables that one would deem to be strongly dependent on the discriminating variable.

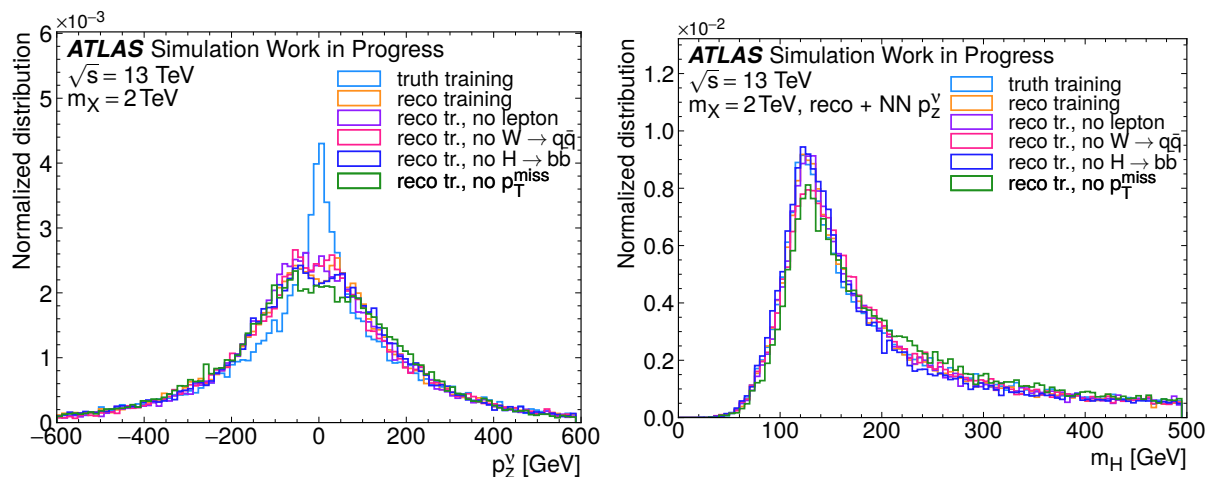


Figure 5.5.: Distributions for p_z^ν (left) and m_H (right). The m_H is calculated from reconstructed variables and NN p_z^ν . Trainings are executed on different sets of reconstructed and truth variables for $m_X = 2$ TeV. The evaluation is on the $m_X = 2$ TeV sample.

5. Analysis

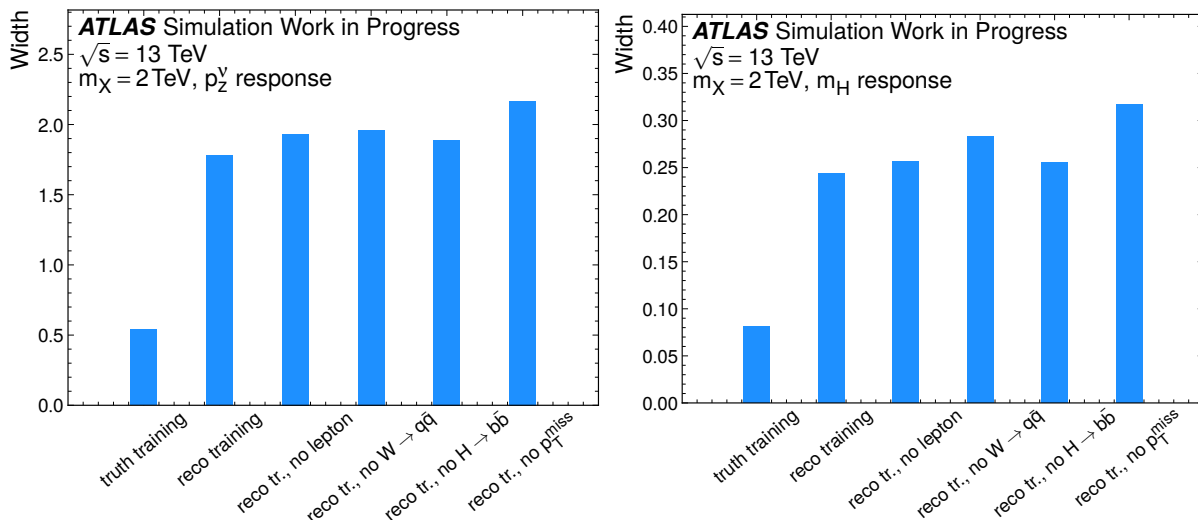


Figure 5.6.: 1σ ranges for distributions of p_z^ν (left) and m_H (right), calculated from reconstructed variables and NN p_z^ν , versus truth p_z^ν and m_H calculated from reconstructed variables and truth p_z^ν . Trainings are executed on different sets of reconstructed and truth variables for $m_X = 2$ TeV. The evaluation is on the $m_X = 2$ TeV sample.

5.5. Differentiation for on-shell and off-shell W bosons

The variables for the W bosons can differ significantly depending on its mass, since the Higgs mass does not support a decay into two on-shell W bosons with $m_H = 125$ GeV and $m_W = 80$ GeV. In general one W boson is produced on-shell and the other one off-shell. The mass of the W boson does not have any influence though, on whether the W boson will decay hadronically or leptonically. As the NN learns on the W_{had} variables, it has to come across two sets of data that correspond to the W_{had} being either on-shell or off-shell. To investigate possible implications on the learning and evaluation process, the events are divided into on-shell and off-shell accordingly. This has been done by cutting on the truth W boson mass of the hadronic W boson. Every W boson with a mass of $m_W \geq 60$ GeV is considered to be on-shell and with a mass of $m_W < 60$ GeV it is considered to be off-shell.

It is also required that each event has exactly one off-shell and one on-shell W boson. Therefore if a W_{had} is identified as being on-shell the W_{lep} is automatically assumed to be off-shell and vice versa, such that the following on- and off-shell statements are in terms of the W_{lep} . The investigation was conducted on a NN trained on events from the mass points $m_X = 0.9$ TeV to $m_X = 4$ TeV. Among the multiple tested scenarios, a training on on-shell and off-shell events combined with an evaluation on only on-shell events and only

off-shell events to see whether there is a preference when reconstructing the p_z^ν by the NN. In the second step a NN was trained exclusively on- or off-shell events and then evaluated on either a combination of on-shell and off-shell events or only on on-shell events for the on-shell training and only on off-shell events for the off-shell training. In the last step the separate trainings and evaluations for either on-shell or off-shell were combined and primarily compared to a mixed training and evaluation, as they have the same amount of events and the most preferable applications as they retain full statistics.

The results are displayed in Figure 5.7 for 1σ interval of the m_H distribution. The distributions for $m_X = 1$ TeV and $m_X = 3$ TeV for the combined training and evaluation method are displayed in Appendix A.4. We can see that there is almost no gain or loss with any of the variations. An exception is the NN with a mixed training and an evaluation on off-shell which shows a particularly bad performance for higher mass points for the m_H distribution. Since the extra steps taken to conduct such a separated approach do not pay off in either necessary computing or performance this approach is not pursued further.

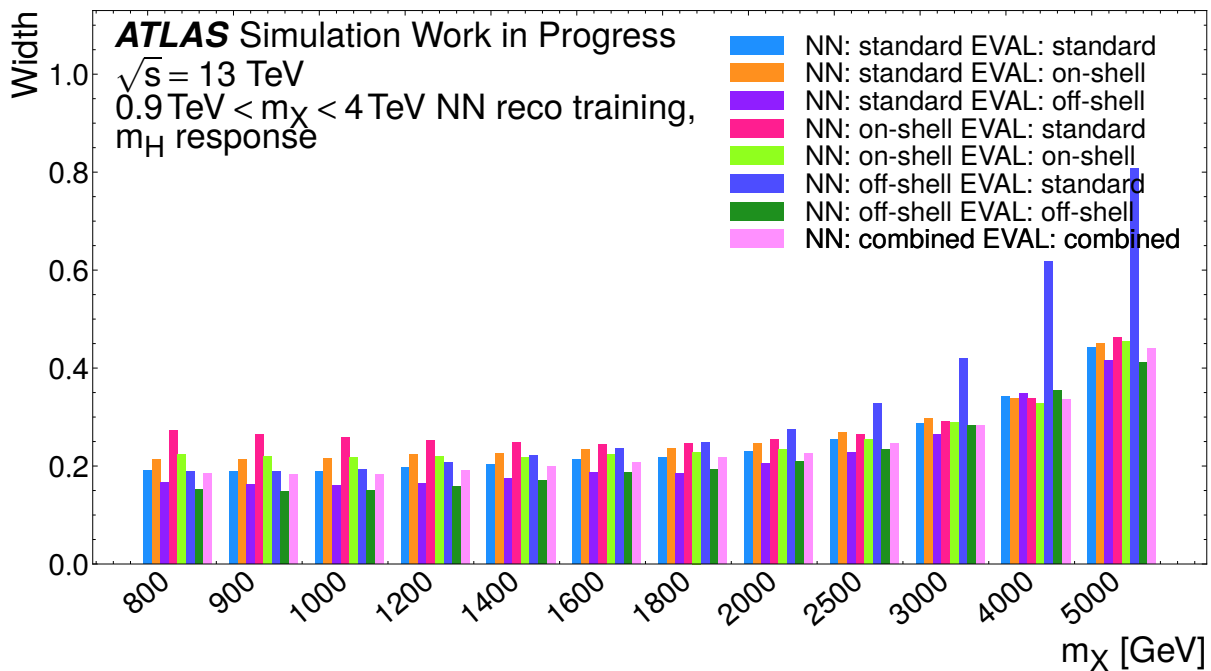


Figure 5.7.: 1σ ranges for m_H calculated from reconstructed variables and NN p_z^ν versus m_H calculated from reconstructed variables and truth p_z^ν for different trainings and evaluations. The trainings and evaluations contain only on-shell, off-shell or both W_{lep} bosons.

5.6. Neural network optimizer

In the next, step the optimizer is configured. The NN's optimizer describes the method with which the NN finds the best composition of weights to reach the best possible approximation of the true p'_z . The commonly used optimizer for the task of regression is stochastic gradient descent (SGD). This methods uses gradient descent to find a minimum of the mean squared error (MSE) between the NN's estimate and the truth p'_z in the phase space that is spanned by the input variables and therefore has a dimension dependent on the number of input variables. Other optimizers use different methods to derive the output with the lowest MSE towards the truth comparison. Examples for other optimizers are Adam, RMSprop and AdaDelta. Although, only Adam is tried next to SGD in an effort to find a suitable optimizer.

The initial reason to change the optimizer or the optimizer settings is that the regression for a NN of all mass points, $m_X = 0.8 \text{ TeV}$ to $m_X = 5 \text{ TeV}$, and all 15 input variables with full statistics failed. But since this NN seemed to be the strongest contender for the final NN the optimizer is adjusted to fit this training. The error is due to the learning rate (LR) being too high. The values are shown in Table 4.1. After trying several LRs, the LR with outstanding performance and a stable training process is 0.0001. Since there are performance improvements to be gained, the other parameters, momentum and decay rate, are also adjusted. Introducing a decay rate in this training led to grave performance losses, though. On the other side, introducing a momentum greatly benefited the training and after trying multiple values for the momentum a value of 0.99 is selected.

Simultaneously, the Adam optimizer is configured. It is given the same learning rate, but Adam does not have a momentum for its process and other variables that can be fed into Adam are not configured. Since it shows a worse performance, it is not chosen as the main optimizer for this study and further configurations are not investigated. The resulting Higgs mass distributions for SGD and Adam can be seen in Figure 5.8. Looking at the p'_z distributions in Figure 5.9, there is a particular feature towards higher mass points. This feature is backtraced to the imbalance of the number of events representing higher and lower mass points. Utilizing that there is an abundance of events, since all mass point are used in the training, it is attempted to lower the number of events representing lower mass points. The mass point with the least events corresponds to the $m_X = 5 \text{ TeV}$ sample. All other mass points are allowed to only contribute the same number of events to the training as this mass point does. This does not completely remove the imbalance since the density of mass points towards lower masses is still significantly higher but it counteracts the effects.

The effects become immediately clear looking at the performance increases in the dis-

tribution for p_z^ν in Figure 5.10. The difference for the m_H distribution in Figure 5.11 is not as pronounced but this is in part because the Higgs mass is already modeled very good. Cutting the events to achieve a better balance between the mass points but retaining as many events as possible seems to be a great handle to improve the learning process. In general, though, one has to add that more events usually impact the training positively or not at all if there are already enough events for the training and the effects of more data diminish.

The SGD optimizer has been chosen in accordance to the results, although the differences between both optimizer are small, making adam a valid choice.

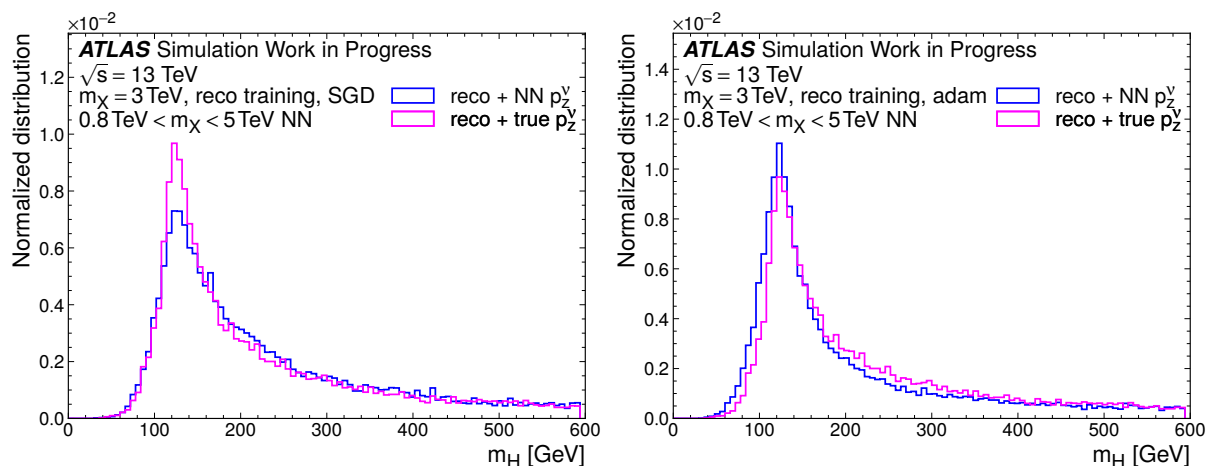


Figure 5.8.: Distributions for m_H calculated from reconstructed variables and NN p_z^ν versus m_H calculated from reconstructed variables and truth p_z^ν . The trainings are conducted with reconstructed variables and and the SGD optimizer (left) and the Adam optimizer (right) of the combined mass points of $m_X = 0.8 \text{ TeV}$ to $m_X = 5 \text{ TeV}$. Evaluation is for $m_X = 3 \text{ TeV}$.

5. Analysis

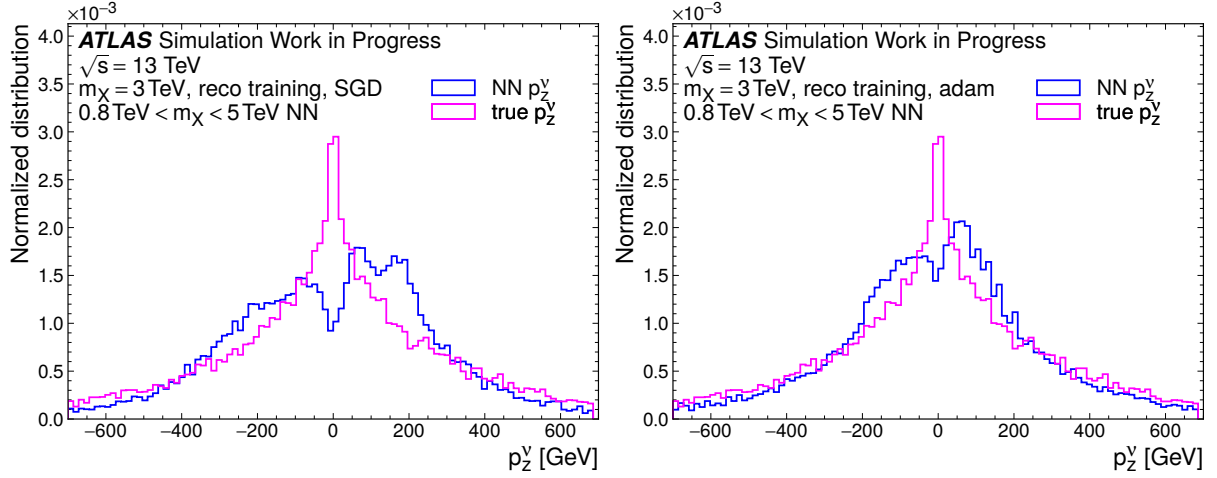


Figure 5.9.: Distributions NN p_z^y versus truth p_z^y . The trainings are conducted with reconstructed variables and and the SGD optimizer (left) and the Adam optimizer (right) of the combined mass points of $m_X = 0.8$ TeV to $m_X = 5$ TeV. Evaluation is for $m_X = 3$ TeV.

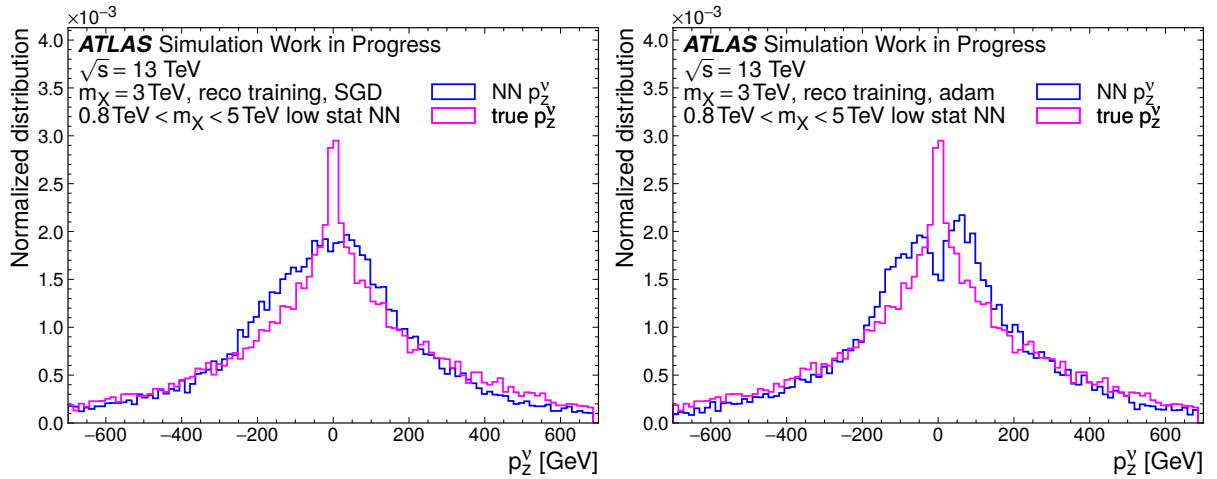


Figure 5.10.: Distributions NN p_z^y versus truth p_z^y . The trainings are conducted with reconstructed variables and and the SGD optimizer (left) and the Adam optimizer (right) of the combined mass points of $m_X = 0.8$ TeV to $m_X = 5$ TeV with lowered statistics. Evaluation is for $m_X = 3$ TeV.

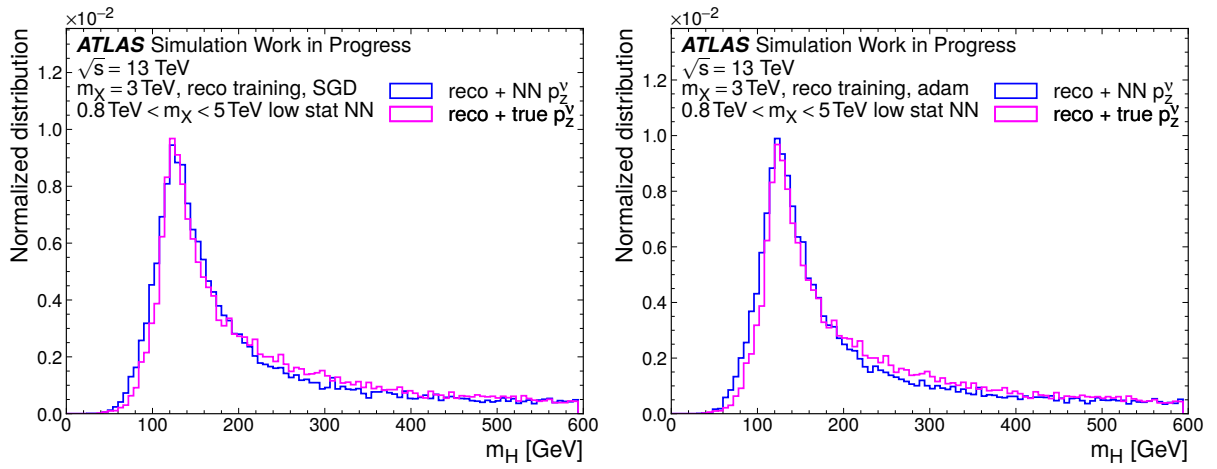


Figure 5.11.: Distributions for m_H calculated from reconstructed variables and NN p_z^ν versus m_H calculated from reconstructed variables and truth p_z^ν . The trainings are conducted with reconstructed variables and the SGD optimizer (left) and the Adam optimizer (right) of the combined mass points of $m_X = 0.8$ TeV to $m_X = 5$ TeV with lowered statistics. Evaluation is for $m_X = 3$ TeV.

5.7. Neural network hyperparameters

Continuing to tune the NN for the training on the full set of variables, the hyperparameters are now under investigation. The examined hyperparameters are the number of neurons and hidden layers as well as the epochs and batch size. Beginning from the starting set of parameters in Table 4.1, one higher and one lower value is tested for the neurons, the hidden layers and the epochs. For the batch size a value of 32 and 64 was tested. Increasing the batch size only has little impact on the performance but benefits the training speed so a batch size of 64 is now used. Similar effects are seen with the neurons, hidden layers and epochs. Higher values do not result in a performance increase and, in the case of the epochs, there even is a very slight decrease in accuracy. Lower values on the other hand also do not change the result noticeably but lower values are usually more desirable since they speed up the training and reduce the necessary computing power. Thus, the lower values are chosen in such cases and the final values can be seen in Table 4.1.

The values are not lowered until there is a performance loss since bringing the NN so close to its boundary can result in unexpected performance losses if the NN is used in slightly different way. Values that could push the NN training over such a boundary are numbers of events and input variables. However, if events, input variables and such are frozen, one can chose to optimize the NN settings a little more for the sake of small performance gains in accuracy and necessary computing power.

5.8. Evaluation on background

Important for the actual usability in an analysis is the NN's performance on background, as one would gain considerably less from a NN that reconstructs background to have similar distribution to signal. This test is conducted after all the preceding changes are made to the training, variables, hyperparameters and the optimizer and, thus, not trained on any background. The already trained NN is simply evaluated on various backgrounds. The tested backgrounds are dijet, $t\bar{t}$ all hadronic, $t\bar{t}$ non all hadronic, $t\bar{t}$ di-lepton, W+Jets and Z+Jets. The results can be seen in Figure 5.12 for m_H and $m_X = 1$ TeV. The samples used to simulate the background events are listed in Appendix B.2.

For m_{HH} , the signal exhibits a good separation of signal and background, which is expected to improve further for higher mass points. The reconstruction of m_H exhibits mixed results since some of the background distributions have a significant overlap with the signal distribution. Despite this overlap, the signal distribution is still separable from the background.

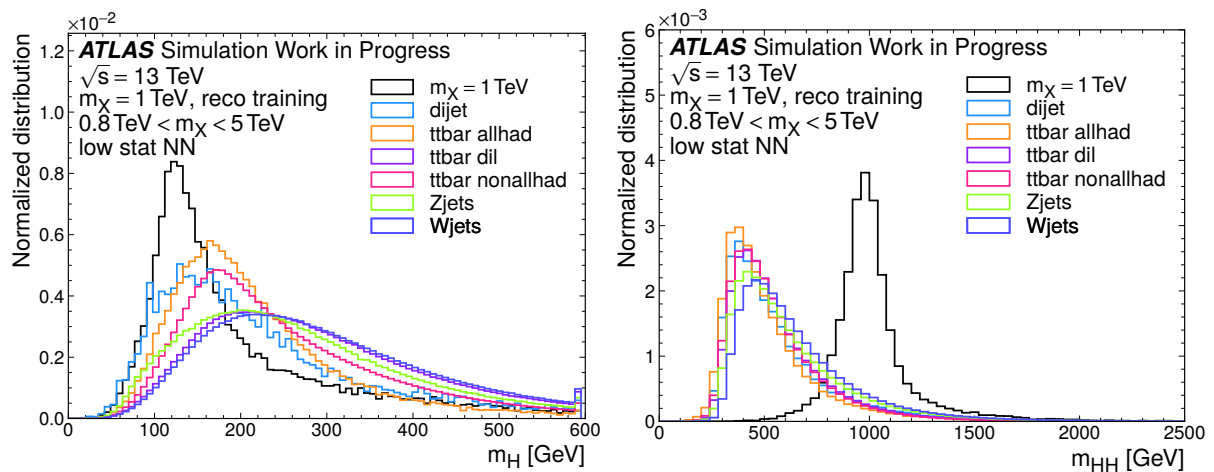


Figure 5.12.: Background distributions on the $m_X = 1$ TeV signal distributions of m_H (left) and m_{HH} (right) built from reconstructed variables and NN p'_z . The training is on the final version of the NN.

6. Conclusion and Outlook

A short summary of the analysis and of the research results is now given. The performance differences between training on reconstructed and truth variables was assessed. The mass points were combined into a single training resulting in a single NN that was used for all masses in the analysis with a performance close to specialized trainings for every single mass point. This includes training on all resonant masses between 0.8 TeV and 5 TeV. The performance benefits of separating the dataset for on- and off-shell W_{Lep} bosons were investigated, and were shown to be negligible. The importance of the respective input variables was examined, with the result being that the NN is able to be trained with a smaller set of input variables without impacting the performance much. The optimizer and the hyperparameters were tuned to fit the final training of one NN on $0.8 \text{ TeV} < m_X < 5 \text{ TeV}$. There the statistics were adjusted to be uniform over all mass points and the optimizer chosen was SGD with momentum. The introduction of a momentum granted a noticeable increase in performance. The impact of the hyperparameters were barely noticeable for big ranges of the respective hyperparameters in terms of performance but lowering the number epochs and neurons for example sped up the training. The final set of hyperparameters and optimizer settings have been summarized in Table 4.1.

The final NN exhibits good performance in terms of the reconstructed m_{HH} and $m_{H \rightarrow WW^*}$, without the background being reconstructed as signal. Compared to other methods of reconstructing, for example $p'_z = 0$, the NN exhibits better resolution for these mass variables, although the difference is small for m_{HH} . The comparisons can be seen in Figure 6.1 for m_{HH} and in Figure 6.2 for $m_{H \rightarrow WW^*}$. The differences in the reconstruction of $m_{H \rightarrow WW^*}$, however, are very noticeable.

Potential tests that are not included in this work are other approaches to machine learning on a fundamental level. Not all possible setups of the NN used in this work were tested. This includes introducing inhomogeneous hidden layers, meaning that that the NN has different numbers neurons per hidden layer. The settings of the hyperparameters and the optimizer are only loosely optimized to make a general argument to whether this is a possibility to improve the NN or not. Possibly some performance could be gained by matching these settings exactly to the used dataset. Using different or more input

6. Conclusion and Outlook

variables, like the number of b-tags in the event could also lead to gains in performance.

The use of a NN in the boosted resonant $HH \rightarrow bbWW^*$ channel with a 1-lepton final state is definitely a viable option and the NN can potentially be applied to any analyses of channels with one neutrino in the final state, as long as there is enough kinematic information in the final state to make a NN training possible. The improved performances for these event reconstructions by NNs could potentially be vital for the search of BSM physics in the future.

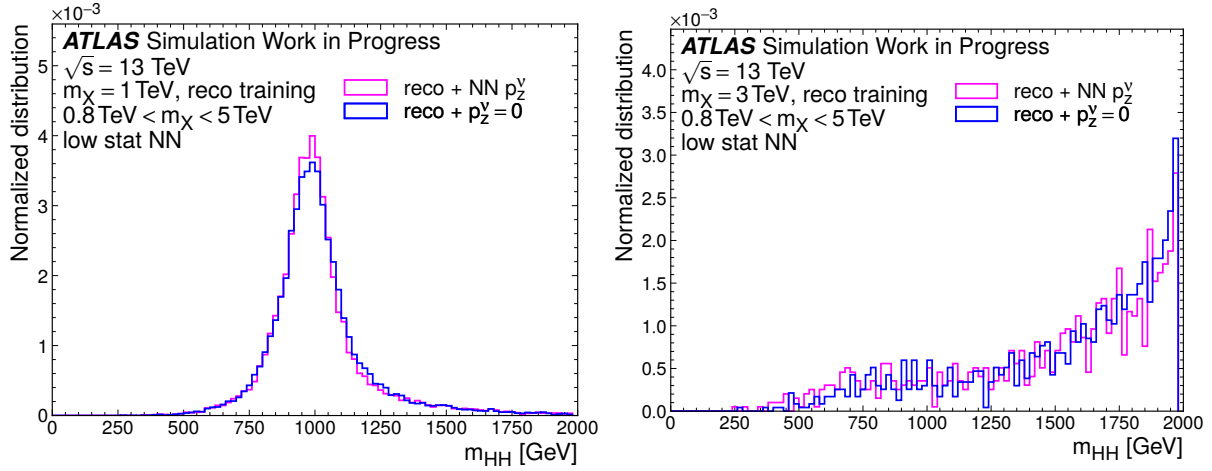


Figure 6.1.: Comparison of distributions for $m_X = 1$ TeV (left) and $m_X = 3$ TeV (right) for calculations from NN p_z^ν and without p_z^ν . Training is on the final model of the NN.

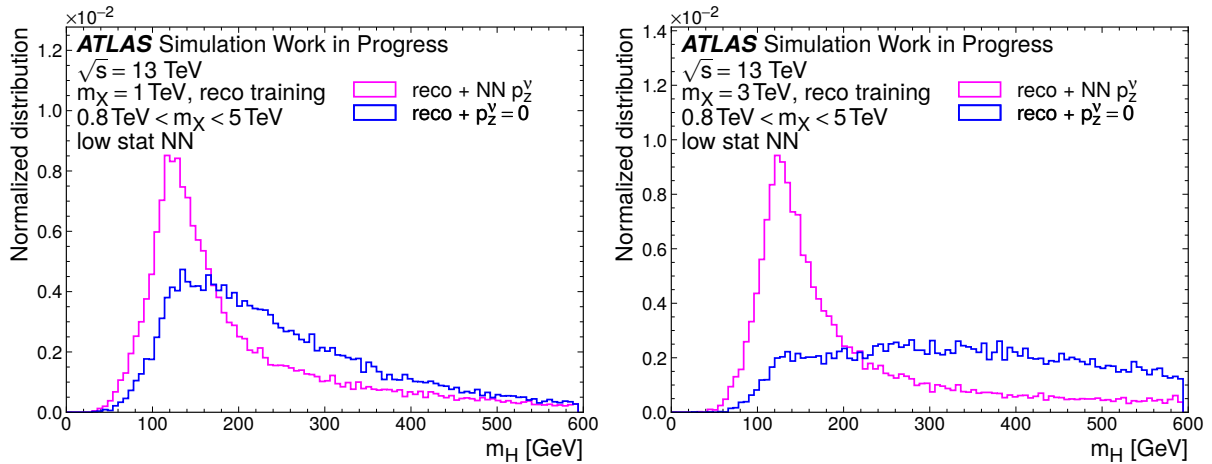


Figure 6.2.: Comparison of distributions for $m_X = 1$ TeV (left) and $m_X = 3$ TeV (right) for calculations from NN p_z^ν and without p_z^ν . Training is on the final model of the NN.

A. Figures

A.1. Distributions for native pairings and training on single mass points

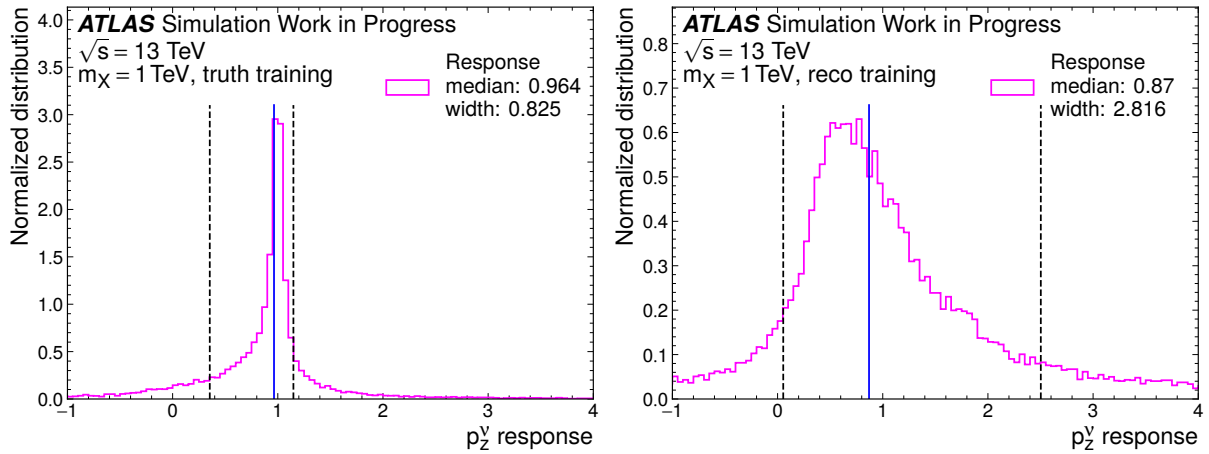


Figure A.1.: Response of p_z^ν . The NN is trained on truth variables (left) and reconstructed variables (right). The black dotted lines indicate the 16th and the 84th percentile and the blue line indicate the median.

A. Figures

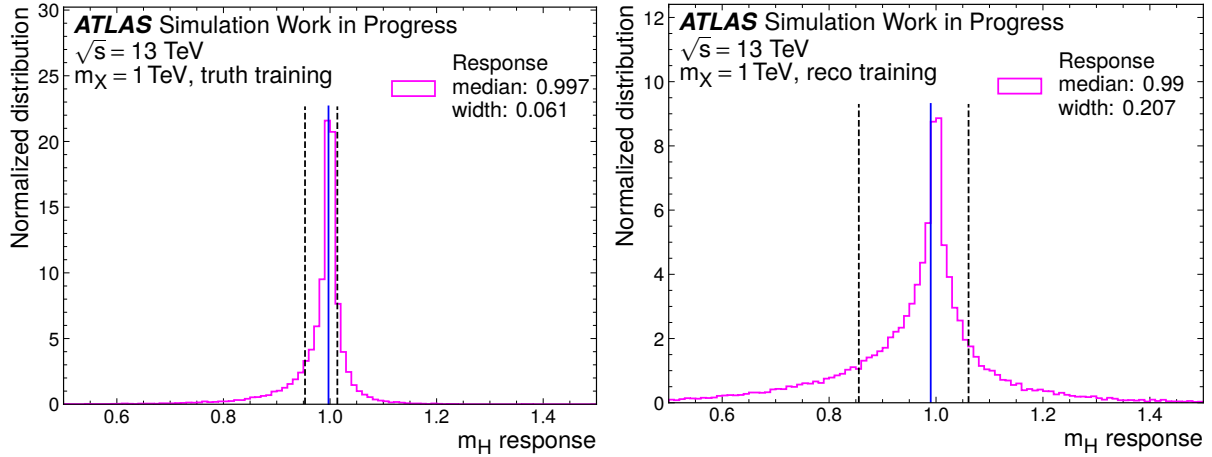


Figure A.2.: Response of m_H calculated from reconstructed variables and NN p_z^ν compared to m_H calculated from reconstructed variables and truth p_z^ν . The NN is trained on truth variables (left) and reconstructed variables (right). The black dotted lines indicate the 16th and the 84th percentile and the blue line indicate the median.

A.2. Distributions for non-native pairings and training on single mass points

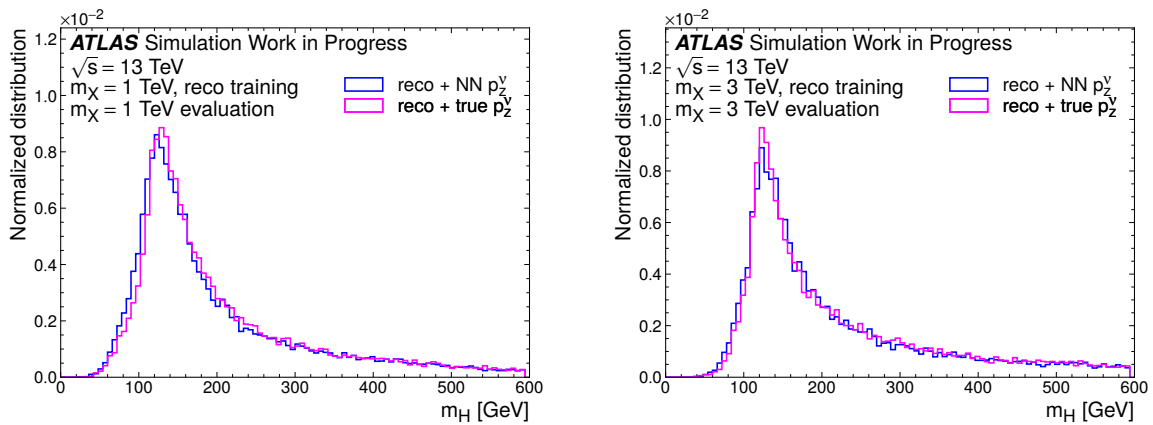


Figure A.3.: Distributions of m_H calculated from reconstructed variables and NN p_z^ν or true p_z^ν . The NN training and evaluation is a native pairing for $m_X = 1$ TeV (left) and $m_X = 3$ TeV (right).

A.2. Distributions for non-native pairings and training on single mass points

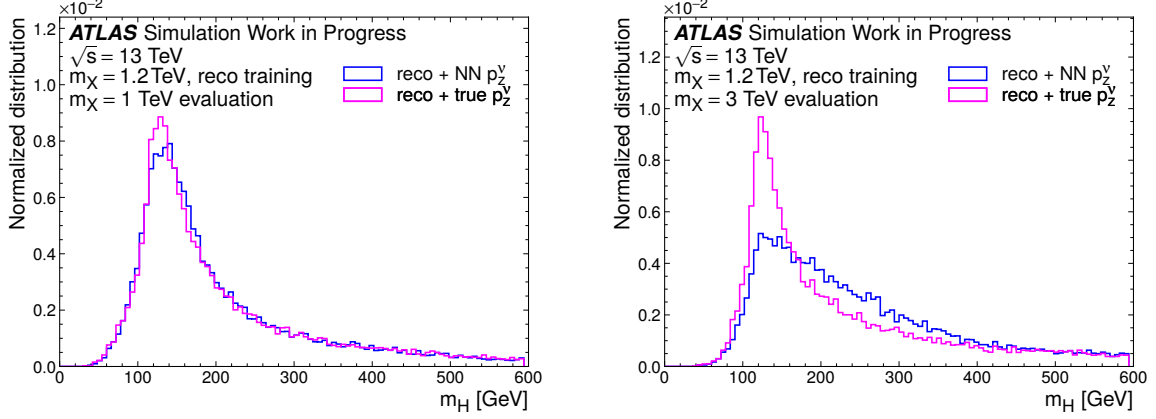


Figure A.4.: Distributions of m_H calculated from reconstructed variables and NN p_z^ν or true p_z^ν . The NN is trained on $m_X = 1.2$ TeV and evaluated for $m_X = 1$ TeV (left) and $m_X = 3$ TeV (right).

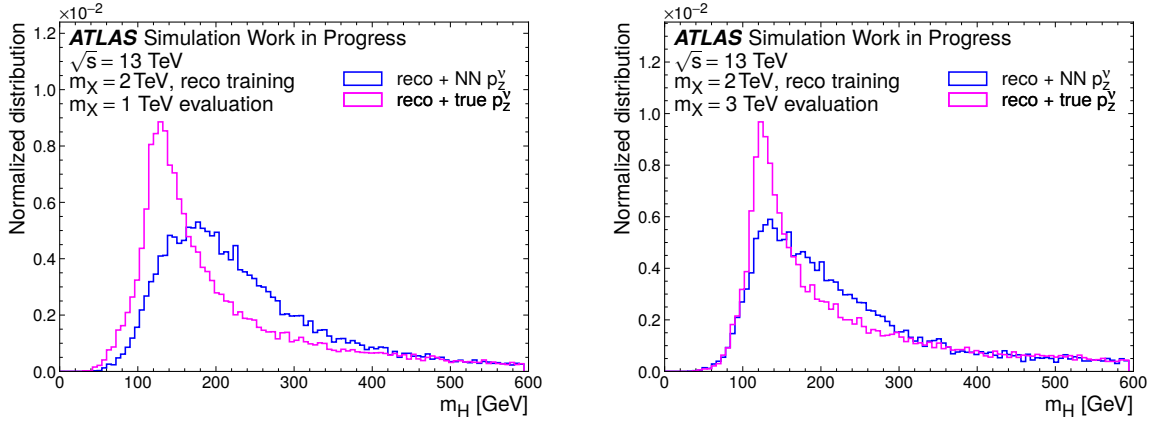


Figure A.5.: Distributions of m_H calculated from reconstructed variables and NN p_z^ν or true p_z^ν . The NN is trained on $m_X = 2$ TeV and evaluated for $m_X = 1$ TeV (left) and $m_X = 3$ TeV (right).

A. Figures

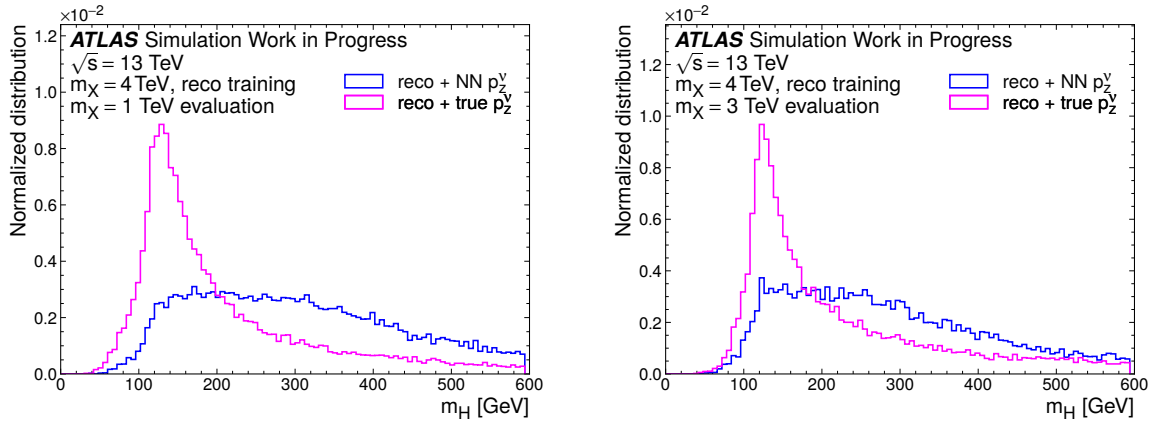


Figure A.6.: Distributions of m_H calculated from reconstructed variables and NN p_z^ν or true p_z^ν . The NN is trained on $m_X = 4$ TeV and evaluated for $m_X = 1$ TeV (left) and $m_X = 3$ TeV (right).

A.3. Distributions for training on multiple mass points

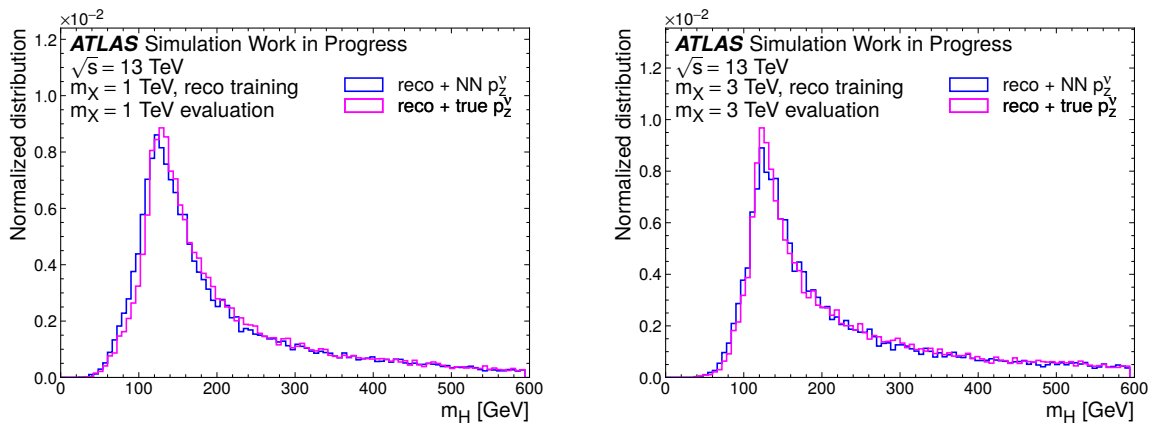


Figure A.7.: Distributions of m_H calculated from reconstructed variables and NN p_z^ν or true p_z^ν . The NN training and evaluation is a native pairing for $m_X = 1$ TeV (left) and $m_X = 3$ TeV (right).

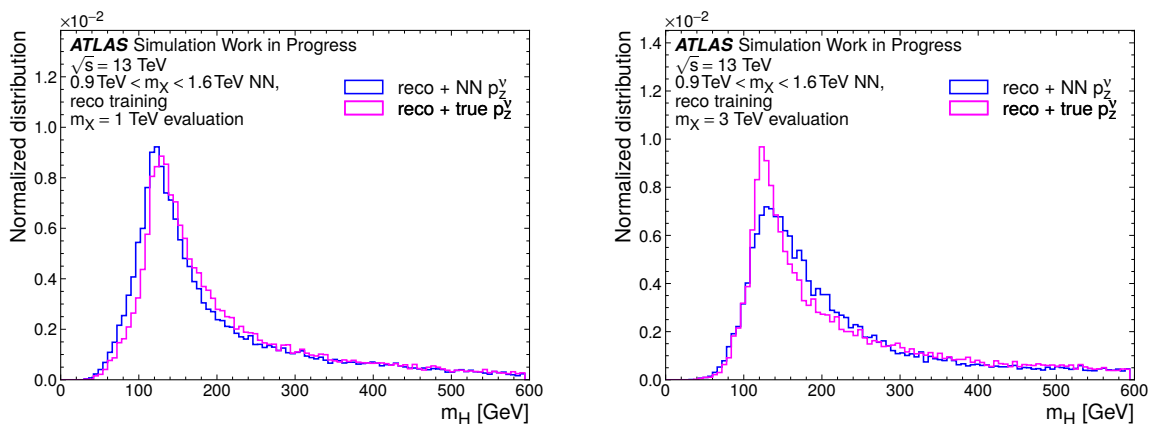


Figure A.8.: Distributions of m_H calculated from reconstructed variables and NN p_z^ν or true p_z^ν . The NN is trained on $0.9 \text{ TeV} < m_X < 1.6 \text{ TeV}$ and evaluated for $m_X = 1$ TeV (left) and $m_X = 3$ TeV (right).

A. Figures

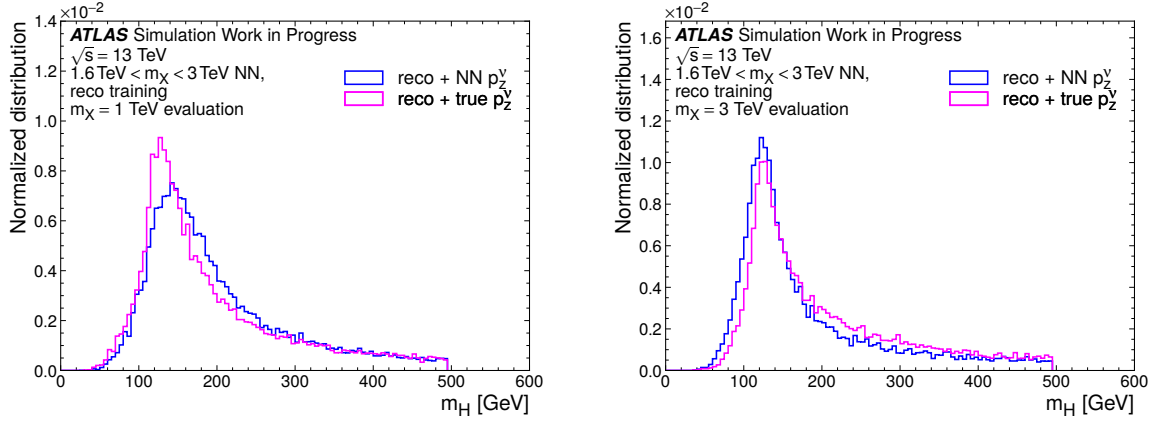


Figure A.9.: Distributions of m_H calculated from reconstructed variables and NN p_z^ν or true p_z^ν . The NN is trained on $1.6 \text{ TeV} < m_X < 3 \text{ TeV}$ and evaluated for $m_X = 1 \text{ TeV}$ (left) and $m_X = 3 \text{ TeV}$ (right).

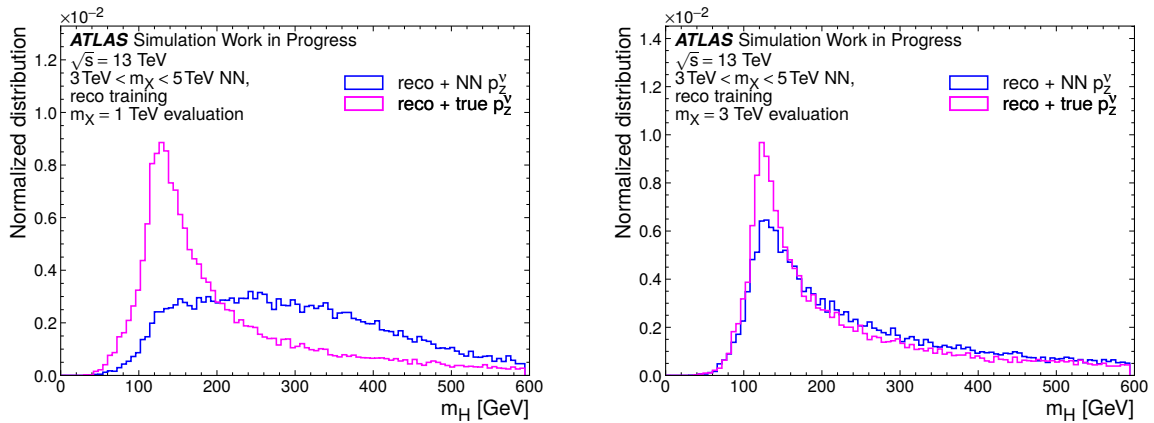


Figure A.10.: Distributions of m_H calculated from reconstructed variables and NN p_z^ν or true p_z^ν . The NN is trained on $3 \text{ TeV} < m_X < 5 \text{ TeV}$ and evaluated for $m_X = 1 \text{ TeV}$ (left) and $m_X = 3 \text{ TeV}$ (right).

A.3. Distributions for training on multiple mass points

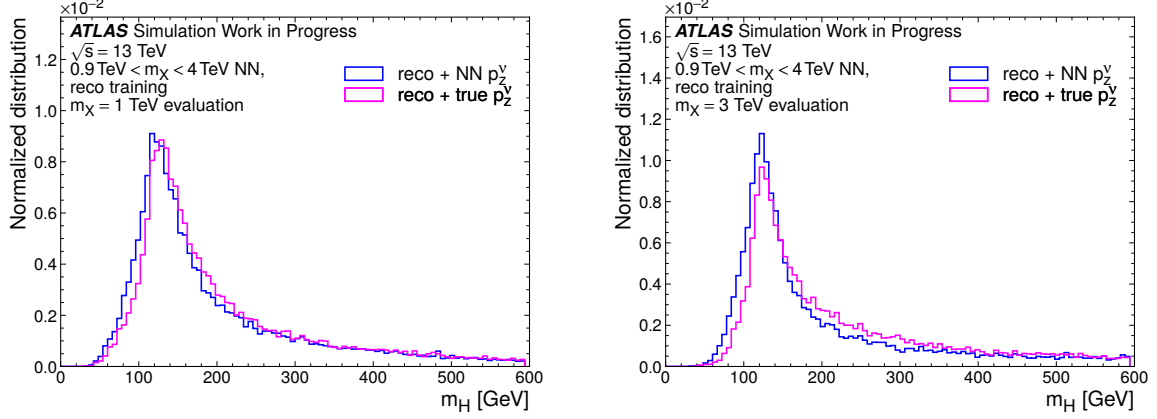


Figure A.11.: Distributions of m_H calculated from reconstructed variables and NN p_z^ν or true p_z^ν . The NN is trained on $0.9 \text{ TeV} < m_X < 4 \text{ TeV}$ and evaluated for $m_X = 1 \text{ TeV}$ (left) and $m_X = 3 \text{ TeV}$ (right).

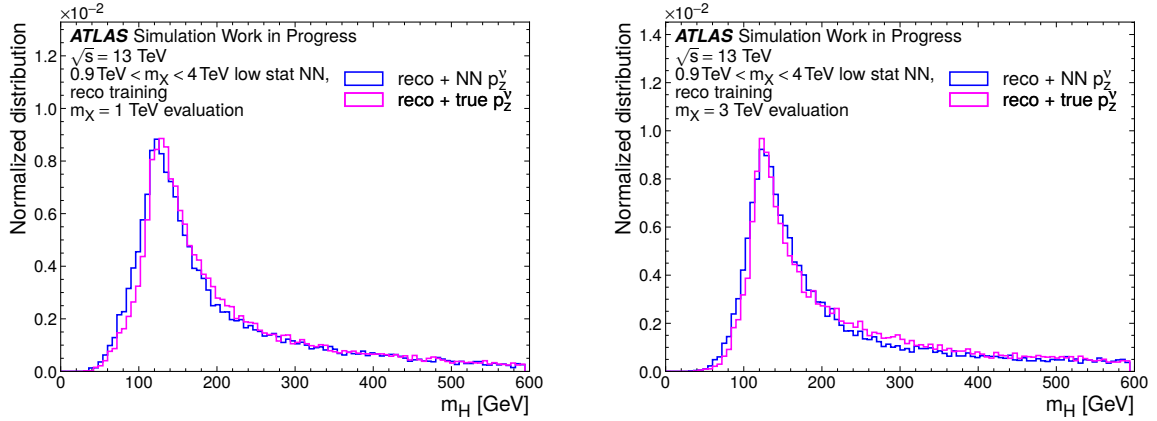


Figure A.12.: Distributions of m_H calculated from reconstructed variables and NN p_z^ν or true p_z^ν . The NN is trained on $0.9 \text{ TeV} < m_X < 1.6 \text{ TeV}$ with lowered statistics and evaluated for $m_X = 1 \text{ TeV}$ (left) and $m_X = 3 \text{ TeV}$ (right).

A. Figures

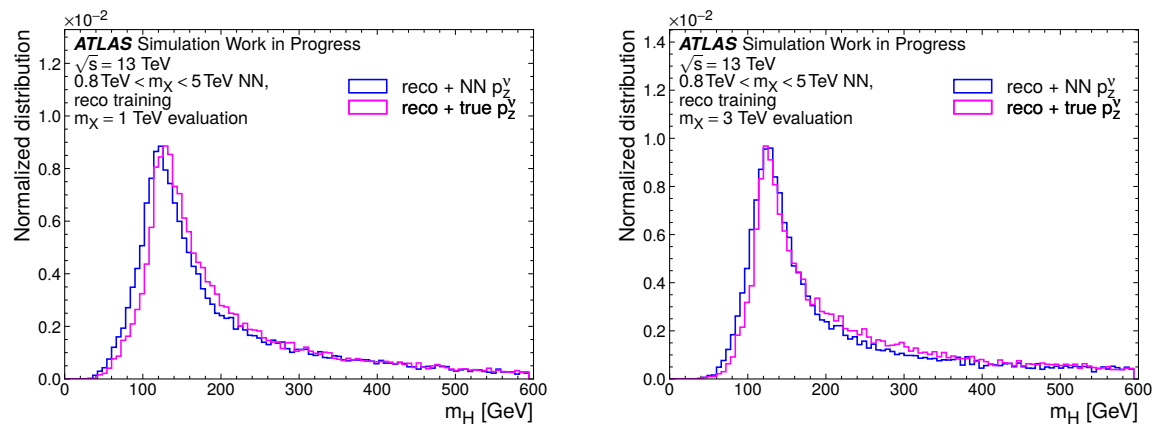


Figure A.13.: Distributions of m_H calculated from reconstructed variables and NN p_z^ν or true p_z^ν . The NN is trained on $0.8 \text{ TeV} < m_X < 5 \text{ TeV}$ and evaluated for $m_X = 1 \text{ TeV}$ (left) and $m_X = 3 \text{ TeV}$ (right).

A.4. Distributions for the differentiation for on- and off-shell W bosons

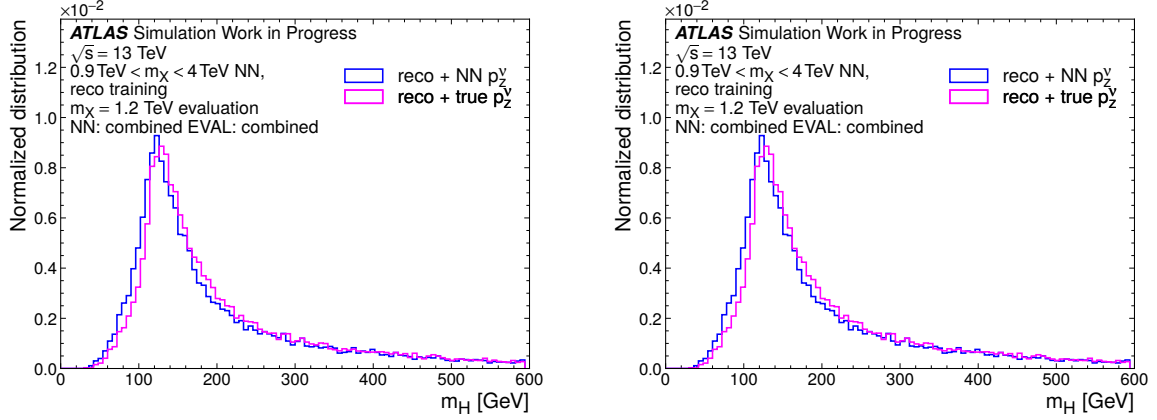


Figure A.14.: Distributions of m_H calculated from reconstructed variables and NN p_z^ν or true p_z^ν . Two NNs are trained on either on-shell or off-shell events and evaluated respectively on only on-shell or off-shell events. The NNs are trained on $0.8 \text{ TeV} < m_X < 5 \text{ TeV}$ and evaluated for $m_X = 1 \text{ TeV}$ (left) and $m_X = 3 \text{ TeV}$ (right). The results of both evaluations are then combined.

B. Tables

B.1. Signal samples

signal
mc16_13TeV.450220.MadGraphHerwig7EvtGen_PDF23LO_X800tohh_WWbb_1lep.evtgen.EVT.e7592
mc16_13TeV.450221.MadGraphHerwig7EvtGen_PDF23LO_X900tohh_WWbb_1lep.evtgen.EVT.e7592
mc16_13TeV.450219.MadGraphHerwig7EvtGen_PDF23LO_X1000tohh_WWbb_1lep.evtgen.EVT.e7329
mc16_13TeV.450222.MadGraphHerwig7EvtGen_PDF23LO_X1200tohh_WWbb_1lep.evtgen.EVT.e7592
mc16_13TeV.450223.MadGraphHerwig7EvtGen_PDF23LO_X1400tohh_WWbb_1lep.evtgen.EVT.e7592
mc16_13TeV.450224.MadGraphHerwig7EvtGen_PDF23LO_X1600tohh_WWbb_1lep.evtgen.EVT.e7592
mc16_13TeV.450225.MadGraphHerwig7EvtGen_PDF23LO_X1800tohh_WWbb_1lep.evtgen.EVT.e7592
mc16_13TeV.450229.MadGraphHerwig7EvtGen_PDF23LO_X2000tohh_WWbb_1lep.evtgen.EVT.e7329
mc16_13TeV.450226.MadGraphHerwig7EvtGen_PDF23LO_X2500tohh_WWbb_1lep.evtgen.EVT.e7592
mc16_13TeV.450239.MadGraphHerwig7EvtGen_PDF23LO_X3000tohh_WWbb_1lep.evtgen.EVT.e7329
mc16_13TeV.450227.MadGraphHerwig7EvtGen_PDF23LO_X4000tohh_WWbb_1lep.evtgen.EVT.e7592
mc16_13TeV.450228.MadGraphHerwig7EvtGen_PDF23LO_X5000tohh_WWbb_1lep.evtgen.EVT.e7592

Table B.1.: Names of the samples that are used for the simulation of the signal for every mass point.

B.2. Background samples

B. Tables

dijet
mc15_13TeV.364712.Pythia8EvtGen_A14NNPDF23LO_jetjet_JZ12WithSW.evgen.EVNT.e7142
mc15_13TeV.364711.Pythia8EvtGen_A14NNPDF23LO_jetjet_JZ11WithSW.evgen.EVNT.e7142
mc15_13TeV.364710.Pythia8EvtGen_A14NNPDF23LO_jetjet_JZ10WithSW.evgen.EVNT.e7142
mc15_13TeV.364709.Pythia8EvtGen_A14NNPDF23LO_jetjet_JZ9WithSW.evgen.EVNT.e7142
mc15_13TeV.364708.Pythia8EvtGen_A14NNPDF23LO_jetjet_JZ8WithSW.evgen.EVNT.e7142
mc15_13TeV.364707.Pythia8EvtGen_A14NNPDF23LO_jetjet_JZ7WithSW.evgen.EVNT.e7142
mc15_13TeV.364706.Pythia8EvtGen_A14NNPDF23LO_jetjet_JZ6WithSW.evgen.EVNT.e7142
mc15_13TeV.364705.Pythia8EvtGen_A14NNPDF23LO_jetjet_JZ5WithSW.evgen.EVNT.e7142
mc15_13TeV.364704.Pythia8EvtGen_A14NNPDF23LO_jetjet_JZ4WithSW.evgen.EVNT.e7142
mc15_13TeV.364703.Pythia8EvtGen_A14NNPDF23LO_jetjet_JZ3WithSW.evgen.EVNT.e7142
mc15_13TeV.364702.Pythia8EvtGen_A14NNPDF23LO_jetjet_JZ2WithSW.evgen.EVNT.e7142
mc15_13TeV.364701.Pythia8EvtGen_A14NNPDF23LO_jetjet_JZ1WithSW.evgen.EVNT.e7142
mc15_13TeV.364700.Pythia8EvtGen_A14NNPDF23LO_jetjet_JZ0WithSW.evgen.EVNT.e7142

Table B.2.: Names of the samples that are used for the simulation of the dijet background.

ttbar
mc15_13TeV.410472.PhPy8EG_A14_ttbar_hdamp258p75_dil.evgen.EVNT.e6348
mc15_13TeV.410471.PhPy8EG_A14_ttbar_hdamp258p75_allhad.evgen.EVNT.e6337
mc15_13TeV.410470.PhPy8EG_A14_ttbar_hdamp258p75_nonallhad.evgen.EVNT.e6337

Table B.3.: Names of the samples that are used for the simulation of the ttbar background.

W+jets	
mc15_13TeV.363483.Sherpa_NNPDF30NNLO_Wenu_Pt2000_E_CMS_BFilter.evgen.EVNT.e4715	
mc15_13TeV.363482.Sherpa_NNPDF30NNLO_Wenu_Pt2000_E_CMS_CFilterBVeto.evgen.EVNT.e4715	
mc15_13TeV.363481.Sherpa_NNPDF30NNLO_Wenu_Pt2000_E_CMS_CVetoBVeto.evgen.EVNT.e4715	
mc15_13TeV.363480.Sherpa_NNPDF30NNLO_Wenu_Pt1000_2000_BFilter.evgen.EVNT.e4715	
mc15_13TeV.363479.Sherpa_NNPDF30NNLO_Wenu_Pt1000_2000_CFilterBVeto.evgen.EVNT.e4715	
mc15_13TeV.363478.Sherpa_NNPDF30NNLO_Wenu_Pt1000_2000_CVetoBVeto.evgen.EVNT.e4715	
mc15_13TeV.363477.Sherpa_NNPDF30NNLO_Wenu_Pt700_1000_BFilter.evgen.EVNT.e4715	
mc15_13TeV.363476.Sherpa_NNPDF30NNLO_Wenu_Pt700_1000_CFilterBVeto.evgen.EVNT.e4715	
mc15_13TeV.363475.Sherpa_NNPDF30NNLO_Wenu_Pt700_1000_CVetoBVeto.evgen.EVNT.e4715	
mc15_13TeV.363474.Sherpa_NNPDF30NNLO_Wenu_Pt500_700_BFilter.evgen.EVNT.e4771	
mc15_13TeV.363473.Sherpa_NNPDF30NNLO_Wenu_Pt500_700_CFilterBVeto.evgen.EVNT.e4715	
mc15_13TeV.363472.Sherpa_NNPDF30NNLO_Wenu_Pt500_700_CVetoBVeto.evgen.EVNT.e4715	
mc15_13TeV.363471.Sherpa_NNPDF30NNLO_Wenu_Pt280_500_BFilter.evgen.EVNT.e4715	
mc15_13TeV.363470.Sherpa_NNPDF30NNLO_Wenu_Pt280_500_CFilterBVeto.evgen.EVNT.e4715	
mc15_13TeV.363469.Sherpa_NNPDF30NNLO_Wenu_Pt280_500_CVetoBVeto.evgen.EVNT.e4715	
mc15_13TeV.363468.Sherpa_NNPDF30NNLO_Wenu_Pt140_280_BFilter.evgen.EVNT.e4715	
mc15_13TeV.363467.Sherpa_NNPDF30NNLO_Wenu_Pt140_280_CFilterBVeto.evgen.EVNT.e4715	
mc15_13TeV.363466.Sherpa_NNPDF30NNLO_Wenu_Pt140_280_CVetoBVeto.evgen.EVNT.e4715	
mc15_13TeV.363465.Sherpa_NNPDF30NNLO_Wenu_Pt70_140_BFilter.evgen.EVNT.e4715	
mc15_13TeV.363464.Sherpa_NNPDF30NNLO_Wenu_Pt70_140_CFilterBVeto.evgen.EVNT.e4715	
mc15_13TeV.363463.Sherpa_NNPDF30NNLO_Wenu_Pt70_140_CVetoBVeto.evgen.EVNT.e4715	
mc15_13TeV.363462.Sherpa_NNPDF30NNLO_Wenu_Pt0_70_BFilter.evgen.EVNT.e4715	
mc15_13TeV.363461.Sherpa_NNPDF30NNLO_Wenu_Pt0_70_CFilterBVeto.evgen.EVNT.e4715	
mc15_13TeV.363460.Sherpa_NNPDF30NNLO_Wenu_Pt0_70_CVetoBVeto.evgen.EVNT.e4715	
mc15_13TeV.363459.Sherpa_NNPDF30NNLO_Wmunu_Pt2000_E_CMS_BFilter.evgen.EVNT.e4715	
mc15_13TeV.363458.Sherpa_NNPDF30NNLO_Wmunu_Pt2000_E_CMS_CFilterBVeto.evgen.EVNT.e4715	
mc15_13TeV.363457.Sherpa_NNPDF30NNLO_Wmunu_Pt2000_E_CMS_CVetoBVeto.evgen.EVNT.e4715	
mc15_13TeV.363456.Sherpa_NNPDF30NNLO_Wmunu_Pt1000_2000_BFilter.evgen.EVNT.e4715	
mc15_13TeV.363455.Sherpa_NNPDF30NNLO_Wmunu_Pt1000_2000_CFilterBVeto.evgen.EVNT.e4715	
mc15_13TeV.363454.Sherpa_NNPDF30NNLO_Wmunu_Pt1000_2000_CVetoBVeto.evgen.EVNT.e4715	
mc15_13TeV.363453.Sherpa_NNPDF30NNLO_Wmunu_Pt700_1000_BFilter.evgen.EVNT.e4715	
mc15_13TeV.363452.Sherpa_NNPDF30NNLO_Wmunu_Pt700_1000_CFilterBVeto.evgen.EVNT.e4715	
mc15_13TeV.363451.Sherpa_NNPDF30NNLO_Wmunu_Pt700_1000_CVetoBVeto.evgen.EVNT.e4715	
mc15_13TeV.363450.Sherpa_NNPDF30NNLO_Wmunu_Pt500_700_BFilter.evgen.EVNT.e4715	
mc15_13TeV.363449.Sherpa_NNPDF30NNLO_Wmunu_Pt500_700_CFilterBVeto.evgen.EVNT.e4715	
mc15_13TeV.363448.Sherpa_NNPDF30NNLO_Wmunu_Pt500_700_CVetoBVeto.evgen.EVNT.e4715	
mc15_13TeV.363447.Sherpa_NNPDF30NNLO_Wmunu_Pt280_500_BFilter.evgen.EVNT.e4715	
mc15_13TeV.363446.Sherpa_NNPDF30NNLO_Wmunu_Pt280_500_CFilterBVeto.evgen.EVNT.e4715	
mc15_13TeV.363445.Sherpa_NNPDF30NNLO_Wmunu_Pt280_500_CVetoBVeto.evgen.EVNT.e4715	
mc15_13TeV.363444.Sherpa_NNPDF30NNLO_Wmunu_Pt140_280_BFilter.evgen.EVNT.e4715	
mc15_13TeV.363443.Sherpa_NNPDF30NNLO_Wmunu_Pt140_280_CFilterBVeto.evgen.EVNT.e4715	
mc15_13TeV.363442.Sherpa_NNPDF30NNLO_Wmunu_Pt140_280_CVetoBVeto.evgen.EVNT.e4715	
mc15_13TeV.363441.Sherpa_NNPDF30NNLO_Wmunu_Pt70_140_BFilter.evgen.EVNT.e4771	
mc15_13TeV.363440.Sherpa_NNPDF30NNLO_Wmunu_Pt70_140_CFilterBVeto.evgen.EVNT.e4715	
mc15_13TeV.363439.Sherpa_NNPDF30NNLO_Wmunu_Pt70_140_CVetoBVeto.evgen.EVNT.e4715	
mc15_13TeV.363438.Sherpa_NNPDF30NNLO_Wmunu_Pt0_70_BFilter.evgen.EVNT.e4715	
mc15_13TeV.363437.Sherpa_NNPDF30NNLO_Wmunu_Pt0_70_CFilterBVeto.evgen.EVNT.e4715	
mc15_13TeV.363436.Sherpa_NNPDF30NNLO_Wmunu_Pt0_70_CVetoBVeto.evgen.EVNT.e4715	
mc15_13TeV.363354.Sherpa_NNPDF30NNLO_Wtaunu_Pt2000_E_CMS_BFilter.evgen.EVNT.e4709	
mc15_13TeV.363353.Sherpa_NNPDF30NNLO_Wtaunu_Pt2000_E_CMS_CFilterBVeto.evgen.EVNT.e4709	
mc15_13TeV.363352.Sherpa_NNPDF30NNLO_Wtaunu_Pt2000_E_CMS_CVetoBVeto.evgen.EVNT.e4709	
mc15_13TeV.363351.Sherpa_NNPDF30NNLO_Wtaunu_Pt1000_2000_BFilter.evgen.EVNT.e4779	
mc15_13TeV.363350.Sherpa_NNPDF30NNLO_Wtaunu_Pt1000_2000_CFilterBVeto.evgen.EVNT.e4709	
mc15_13TeV.363349.Sherpa_NNPDF30NNLO_Wtaunu_Pt1000_2000_CVetoBVeto.evgen.EVNT.e4709	
mc15_13TeV.363348.Sherpa_NNPDF30NNLO_Wtaunu_Pt700_1000_BFilter.evgen.EVNT.e4779	
mc15_13TeV.363347.Sherpa_NNPDF30NNLO_Wtaunu_Pt700_1000_CFilterBVeto.evgen.EVNT.e4709	
mc15_13TeV.363346.Sherpa_NNPDF30NNLO_Wtaunu_Pt700_1000_CVetoBVeto.evgen.EVNT.e4709	
mc15_13TeV.363345.Sherpa_NNPDF30NNLO_Wtaunu_Pt500_700_BFilter.evgen.EVNT.e4779	
mc15_13TeV.363344.Sherpa_NNPDF30NNLO_Wtaunu_Pt500_700_CFilterBVeto.evgen.EVNT.e4709	
mc15_13TeV.363343.Sherpa_NNPDF30NNLO_Wtaunu_Pt500_700_CVetoBVeto.evgen.EVNT.e4709	
mc15_13TeV.363342.Sherpa_NNPDF30NNLO_Wtaunu_Pt280_500_BFilter.evgen.EVNT.e4779	
mc15_13TeV.363341.Sherpa_NNPDF30NNLO_Wtaunu_Pt280_500_CFilterBVeto.evgen.EVNT.e4779	
mc15_13TeV.363340.Sherpa_NNPDF30NNLO_Wtaunu_Pt280_500_CVetoBVeto.evgen.EVNT.e4709	
mc15_13TeV.363339.Sherpa_NNPDF30NNLO_Wtaunu_Pt140_280_BFilter.evgen.EVNT.e4709	
mc15_13TeV.363338.Sherpa_NNPDF30NNLO_Wtaunu_Pt140_280_CFilterBVeto.evgen.EVNT.e4709	
mc15_13TeV.363337.Sherpa_NNPDF30NNLO_Wtaunu_Pt140_280_CVetoBVeto.evgen.EVNT.e4709	
mc15_13TeV.363336.Sherpa_NNPDF30NNLO_Wtaunu_Pt70_140_BFilter.evgen.EVNT.e4779	
mc15_13TeV.363335.Sherpa_NNPDF30NNLO_Wtaunu_Pt70_140_CFilterBVeto.evgen.EVNT.e4709	
mc15_13TeV.363334.Sherpa_NNPDF30NNLO_Wtaunu_Pt70_140_CVetoBVeto.evgen.EVNT.e4709	
mc15_13TeV.363333.Sherpa_NNPDF30NNLO_Wtaunu_Pt0_70_BFilter.evgen.EVNT.e4709	
mc15_13TeV.363332.Sherpa_NNPDF30NNLO_Wtaunu_Pt0_70_CFilterBVeto.evgen.EVNT.e4709	
mc15_13TeV.363331.Sherpa_NNPDF30NNLO_Wtaunu_Pt0_70_CVetoBVeto.evgen.EVNT.e4709	

Table B.4.: Names of the samples that are used for the simulation of the W+jets background.

B. Tables

Z+jets	
mc15_13TeV.364361.Sherpa_221_NNPDF30NNLO_Zee_Mll2Ml_MAXHTPTV140_280.evgen.EVNT.e6544	
mc15_13TeV.364358.Sherpa_221_NNPDF30NNLO_Zee_Mll2Ml_MAXHTPTV70_140.evgen.EVNT.e6544	
mc15_13TeV.364280.Sherpa_221_NNPDF30NNLO_Zee_Mll2Ml_MAXHTPTV280_E_CMS.evgen.EVNT.e6037	
mc15_13TeV.364237.Sherpa_221_NNPDF30NNLO_Zee_MAXHTPTV1000_E_CMS_Mll130.evgen.EVNT.e5750	
mc15_13TeV.364236.Sherpa_221_NNPDF30NNLO_Zee_MAXHTPTV500_1000_Mll130.evgen.EVNT.e5750	
mc15_13TeV.364235.Sherpa_221_NNPDF30NNLO_Zee_MAXHTPTV280_500_Mll130.evgen.EVNT.e5750	
mc15_13TeV.364219.Sherpa_221_NNPDF30NNLO_Zee_PTV1000_E_CMS.evgen.EVNT.e5626	
mc15_13TeV.364218.Sherpa_221_NNPDF30NNLO_Zee_PTV500_1000.evgen.EVNT.e5626	
mc15_13TeV.364127.Sherpa_221_NNPDF30NNLO_Zee_MAXHTPTV1000_E_CMS.evgen.EVNT.e5299	
mc15_13TeV.364126.Sherpa_221_NNPDF30NNLO_Zee_MAXHTPTV500_1000.evgen.EVNT.e5299	
mc15_13TeV.364125.Sherpa_221_NNPDF30NNLO_Zee_MAXHTPTV280_500_BFilter.evgen.EVNT.e5299	
mc15_13TeV.364124.Sherpa_221_NNPDF30NNLO_Zee_MAXHTPTV280_500_CFilterBVeto.evgen.EVNT.e5299	
mc15_13TeV.364123.Sherpa_221_NNPDF30NNLO_Zee_MAXHTPTV280_500_CVetoBVeto.evgen.EVNT.e5299	
mc15_13TeV.364122.Sherpa_221_NNPDF30NNLO_Zee_MAXHTPTV140_280_BFilter.evgen.EVNT.e5299	
mc15_13TeV.364121.Sherpa_221_NNPDF30NNLO_Zee_MAXHTPTV140_280_CFilterBVeto.evgen.EVNT.e5299	
mc15_13TeV.364120.Sherpa_221_NNPDF30NNLO_Zee_MAXHTPTV140_280_CVetoBVeto.evgen.EVNT.e5299	
mc15_13TeV.364119.Sherpa_221_NNPDF30NNLO_Zee_MAXHTPTV70_140_BFilter.evgen.EVNT.e5299	
mc15_13TeV.364118.Sherpa_221_NNPDF30NNLO_Zee_MAXHTPTV70_140_CFilterBVeto.evgen.EVNT.e5299	
mc15_13TeV.364117.Sherpa_221_NNPDF30NNLO_Zee_MAXHTPTV70_140_CVetoBVeto.evgen.EVNT.e5299	
mc15_13TeV.364116.Sherpa_221_NNPDF30NNLO_Zee_MAXHTPTV0_70_BFilter.evgen.EVNT.e5299	
mc15_13TeV.364115.Sherpa_221_NNPDF30NNLO_Zee_MAXHTPTV0_70_CFilterBVeto.evgen.EVNT.e5299	
mc15_13TeV.364114.Sherpa_221_NNPDF30NNLO_Zee_MAXHTPTV0_70_CVetoBVeto.evgen.EVNT.e5299	
mc15_13TeV.364498.Sherpa_221_NNPDF30NNLO_Zmumu_MAXHTPTV1000_E_CMS_noHadMPI.evgen.EVNT.e6405	
mc15_13TeV.364497.Sherpa_221_NNPDF30NNLO_Zmumu_MAXHTPTV500_1000_noHadMPI.evgen.EVNT.e6405	
mc15_13TeV.364496.Sherpa_221_NNPDF30NNLO_Zmumu_MAXHTPTV280_500_noHadMPI.evgen.EVNT.e6405	
mc15_13TeV.364495.Sherpa_221_NNPDF30NNLO_Zmumu_MAXHTPTV140_280_noHadMPI.evgen.EVNT.e6405	
mc15_13TeV.364494.Sherpa_221_NNPDF30NNLO_Zmumu_MAXHTPTV70_140_noHadMPI.evgen.EVNT.e6405	
mc15_13TeV.364493.Sherpa_221_NNPDF30NNLO_Zmumu_MAXHTPTV0_70_noHadMPI.evgen.EVNT.e6405	
mc15_13TeV.364362.Sherpa_221_NNPDF30NNLO_Zmumu_Mll2Ml_MAXHTPTV140_280.evgen.EVNT.e6544	
mc15_13TeV.364359.Sherpa_221_NNPDF30NNLO_Zmumu_Mll2Ml_MAXHTPTV70_140.evgen.EVNT.e6544	
mc15_13TeV.364281.Sherpa_221_NNPDF30NNLO_Zmumu_Mll2Ml_MAXHTPTV280_E_CMS.evgen.EVNT.e6037	
mc15_13TeV.364233.Sherpa_221_NNPDF30NNLO_Zmumu_MAXHTPTV1000_E_CMS_Mll130.evgen.EVNT.e5750	
mc15_13TeV.364232.Sherpa_221_NNPDF30NNLO_Zmumu_MAXHTPTV500_1000_Mll130.evgen.EVNT.e5750	
mc15_13TeV.364231.Sherpa_221_NNPDF30NNLO_Zmumu_MAXHTPTV280_500_Mll130.evgen.EVNT.e5750	
mc15_13TeV.364217.Sherpa_221_NNPDF30NNLO_Zmumu_PTV1000_E_CMS.evgen.EVNT.e5626	
mc15_13TeV.364216.Sherpa_221_NNPDF30NNLO_Zmumu_PTV500_1000.evgen.EVNT.e5626	
mc15_13TeV.364113.Sherpa_221_NNPDF30NNLO_Zmumu_MAXHTPTV1000_E_CMS.evgen.EVNT.e5271	
mc15_13TeV.364112.Sherpa_221_NNPDF30NNLO_Zmumu_MAXHTPTV500_1000.evgen.EVNT.e5271	
mc15_13TeV.364111.Sherpa_221_NNPDF30NNLO_Zmumu_MAXHTPTV280_500_BFilter.evgen.EVNT.e5271	
mc15_13TeV.364110.Sherpa_221_NNPDF30NNLO_Zmumu_MAXHTPTV280_500_CFilterBVeto.evgen.EVNT.e5271	
mc15_13TeV.364109.Sherpa_221_NNPDF30NNLO_Zmumu_MAXHTPTV280_500_CVetoBVeto.evgen.EVNT.e5271	
mc15_13TeV.364108.Sherpa_221_NNPDF30NNLO_Zmumu_MAXHTPTV140_280_BFilter.evgen.EVNT.e5271	
mc15_13TeV.364107.Sherpa_221_NNPDF30NNLO_Zmumu_MAXHTPTV140_280_CFilterBVeto.evgen.EVNT.e5271	
mc15_13TeV.364106.Sherpa_221_NNPDF30NNLO_Zmumu_MAXHTPTV140_280_CVetoBVeto.evgen.EVNT.e5271	
mc15_13TeV.364105.Sherpa_221_NNPDF30NNLO_Zmumu_MAXHTPTV70_140_BFilter.evgen.EVNT.e5271	
mc15_13TeV.364104.Sherpa_221_NNPDF30NNLO_Zmumu_MAXHTPTV70_140_CFilterBVeto.evgen.EVNT.e5271	
mc15_13TeV.364103.Sherpa_221_NNPDF30NNLO_Zmumu_MAXHTPTV70_140_CVetoBVeto.evgen.EVNT.e5271	
mc15_13TeV.364102.Sherpa_221_NNPDF30NNLO_Zmumu_MAXHTPTV0_70_BFilter.evgen.EVNT.e5271	
mc15_13TeV.364101.Sherpa_221_NNPDF30NNLO_Zmumu_MAXHTPTV0_70_CFilterBVeto.evgen.EVNT.e5271	
mc15_13TeV.364100.Sherpa_221_NNPDF30NNLO_Zmumu_MAXHTPTV0_70_CVetoBVeto.evgen.EVNT.e5271	
mc15_13TeV.364363.Sherpa_221_NNPDF30NNLO_Ztautau_Mll2Ml_MAXHTPTV140_280.evgen.EVNT.e6544	
mc15_13TeV.364360.Sherpa_221_NNPDF30NNLO_Ztautau_Mll2Ml_MAXHTPTV70_140.evgen.EVNT.e6544	
mc15_13TeV.364282.Sherpa_221_NNPDF30NNLO_Ztautau_Mll2Ml_MAXHTPTV280_E_CMS.evgen.EVNT.e6037	
mc15_13TeV.364221.Sherpa_221_NNPDF30NNLO_Ztautau_PTV1000_E_CMS.evgen.EVNT.e5626	
mc15_13TeV.364220.Sherpa_221_NNPDF30NNLO_Ztautau_PTV500_1000.evgen.EVNT.e5626	
mc15_13TeV.364141.Sherpa_221_NNPDF30NNLO_Ztautau_MAXHTPTV1000_E_CMS.evgen.EVNT.e5307	
mc15_13TeV.364140.Sherpa_221_NNPDF30NNLO_Ztautau_MAXHTPTV500_1000.evgen.EVNT.e5307	
mc15_13TeV.364139.Sherpa_221_NNPDF30NNLO_Ztautau_MAXHTPTV280_500_BFilter.evgen.EVNT.e5313	
mc15_13TeV.364138.Sherpa_221_NNPDF30NNLO_Ztautau_MAXHTPTV280_500_CFilterBVeto.evgen.EVNT.e5313	
mc15_13TeV.364137.Sherpa_221_NNPDF30NNLO_Ztautau_MAXHTPTV280_500_CVetoBVeto.evgen.EVNT.e5307	
mc15_13TeV.364136.Sherpa_221_NNPDF30NNLO_Ztautau_MAXHTPTV140_280_BFilter.evgen.EVNT.e5307	
mc15_13TeV.364135.Sherpa_221_NNPDF30NNLO_Ztautau_MAXHTPTV140_280_CFilterBVeto.evgen.EVNT.e5307	
mc15_13TeV.364134.Sherpa_221_NNPDF30NNLO_Ztautau_MAXHTPTV140_280_CVetoBVeto.evgen.EVNT.e5307	
mc15_13TeV.364133.Sherpa_221_NNPDF30NNLO_Ztautau_MAXHTPTV70_140_BFilter.evgen.EVNT.e5307	
mc15_13TeV.364132.Sherpa_221_NNPDF30NNLO_Ztautau_MAXHTPTV70_140_CFilterBVeto.evgen.EVNT.e5307	
mc15_13TeV.364131.Sherpa_221_NNPDF30NNLO_Ztautau_MAXHTPTV70_140_CVetoBVeto.evgen.EVNT.e5307	
mc15_13TeV.364130.Sherpa_221_NNPDF30NNLO_Ztautau_MAXHTPTV0_70_BFilter.evgen.EVNT.e5307	
mc15_13TeV.364129.Sherpa_221_NNPDF30NNLO_Ztautau_MAXHTPTV0_70_CFilterBVeto.evgen.EVNT.e5307	
mc15_13TeV.364128.Sherpa_221_NNPDF30NNLO_Ztautau_MAXHTPTV0_70_CVetoBVeto.evgen.EVNT.e5307	

Table B.5.: Names of the samples that are used for the simulation of the Z+jets background.

Bibliography

- [1] S. Weinberg, *A Model of Leptons*, Phys. Rev. Lett. **19**, 1264 (1967)
- [2] A. Salam, *Weak and Electromagnetic Interactions*, Conf. Proc. C **680519**, 367 (1968)
- [3] S. L. Glashow, S. Weinberg, *Natural Conservation Laws for Neutral Currents*, Phys. Rev. D **15**, 1958 (1977)
- [4] S. Weinberg, *Implications of Dynamical Symmetry Breaking*, Phys. Rev. D **13**, 974 (1976), [Addendum: Phys.Rev.D 19, 1277–1280 (1979)]
- [5] G. Altarelli, *A QCD primer*, AIP Conf. Proc. **631(1)**, 70 (2002)
- [6] S. Schael et al. (ALEPH, DELPHI, L3, OPAL, SLD, LEP Electroweak Working Group, SLD Electroweak Group, SLD Heavy Flavour Group), *Precision electroweak measurements on the Z resonance*, Phys. Rept. **427**, 257 (2006)
- [7] M. Lubej, *The Standard Model* (2020), online; accessed August 14, 2020, URL https://github.com/mlubej/pet_projects/blob/master/standard-model/SM.pdf
- [8] J. Goldstone, A. Salam, S. Weinberg, *Broken Symmetries*, Phys. Rev. **127**, 965 (1962)
- [9] NIST, *The NIST Reference on Constants, Units, and Uncertainty* (2019), online; accessed October 21, 2020, URL <https://physics.nist.gov/cgi-bin/cuu/Value?sin2th>
- [10] ATLAS Collaboration, *Observation of a new particle in the search for the Standard Model Higgs boson with the ATLAS detector at the LHC*, Physics Letters B **716** (2012)
- [11] B. Di Micco et al., *Higgs Boson Pair Production at Colliders: Status and Perspectives* (2019), arXiv:1910.00012[hep-ph]
- [12] LHC Higgs Cross Section Working Group, *Handbook of LHC Higgs Cross Sections: 4. Deciphering the Nature of the Higgs Sector* (2016), arXiv:1610.07922 [hep-ph], CERN-2017-002-M, CERN-2017-002, arXiv:1610.07922[hep-ph],

Bibliography

- [13] J. Dolan, C. Englert, M. Spannowsky, *Higgs self-coupling measurements at the LHC*, JHEP **10**, 112 (2012)
- [14] R. Tanaka, *Standard Model Higgs boson decay branching ratios and total width* (2016), online; accessed August 23, 2020, URL <https://twiki.cern.ch/twiki/bin/view/LHCPhysics/LHCHXSWGCrossSectionsFigures>
- [15] G.C. Branco et al., *Theory and phenomenology of two-Higgs-doublet models*, Phys. Rept. **516**, 1 (2012)
- [16] H. Haber, G. Kane, *The search for supersymmetry: Probing physics beyond the standard model*, Physics Reports **117(2)**, 75 (1985)
- [17] E. Mobs, *The CERN accelerator complex - 2019. Complexe des accélérateurs du CERN - 2019* (2019), general Photo, URL <https://cds.cern.ch/record/2684277>
- [18] ATLAS Collaboration (ATLAS), *The ATLAS Experiment at the CERN Large Hadron Collider*, JINST **3**, S08003 (2008)

Acknowledgement

It has been a blast. Working on and with today's physics has opened a new realm for me and I can already feel the addiction. Grinding through the nights while programming and writing with happiness and dedication showed me that I have found where I belong. But I not only found awesome physics but also awesome people:

Stan, you are such a wholehearted man, who brings a great energy and positivity to those around you, including me. You are dedicating so much of your time to check up on everyone in your group and ensure that everyone gets the help and guidance they need. And I believe that passing on your inspiration and love for awesome physics is one of your greatest qualities and contribution to physics. The second great quality of yours is that you are able and willing to endure even my worst jokes and memes in the meetings and mails. The third greatest quality is of course that you even laughed at some of them. But jokes aside, I am very grateful to you for this opportunity, this experience and the man you are.

Jason, you are just awesome. Although your schedule seemingly does not include free time, you always found a way to squeeze me in and help me with my everyday problems even before the thesis. For that you earned my respect and gratitude. You taught me everything from the rubber-ducky to the ATLAS detector and all that there is in between. I hope we will have many more conversations about awesome physics in the future. I hope I could bring some smiles into your day with Mini-Jason and the likes. And, because you are always working, I want you now - yes, while you read this - to take a small break and appreciate the moment and maybe even give Maxwell a pet. Talk to you later!

Kira, you are a great teacher since the beginning when you were tutoring me until the end. In fact, your research and you being in Stan's group played a big role in bringing me into this mess. For this and your patience, which I know I have tested some times (I am sorry :D), I want to thank you. I wish you all the best for the future, especially for your PhD, which I know you will rock.

Meine Familie soll hier natürlich auch nicht unerwähnt bleiben. Mama, Papa, Oma, ich weiß, dass es nicht immer leicht war, mich in die Ferne zum Studieren ziehen zu lassen,

Bibliography

aber ich weiß auch, dass ihr mich immer so gut es geht unterstützt habt und werdet. Diese Arbeit ist einer der ersten Meilensteine auf meinem Weg und ich weiß ihr werdet, noch einige miterleben, also platzt nicht gleich vor Stolz. Hab euch ganz doll lieb.

Meine Freunde sind offensichtlich auch mit von der Partie. Ob von der Uni oder aus Soltau – Ihr seid die besten. Am Anfang kann man sich das nie so richtig vorstellen, aber jetzt sind wir alle auf unserem Weg und quer in Deutschland verteilt, aber die Erinnerungen an unsere gemeinsamen Zeiten sind unschlagbar. Und da wir es alle geschafft haben, uns immer wieder über den Weg zu laufen: Bis bald, Freunde.

This thesis may finally come to an end but I want you and the physics community to know that this shall not be the last time you saw my name on a thesis as I plan to do a lot more awesome physics!

Peace out!

Yannik

Erklärung

nach §13(9) der Prüfungsordnung für den Bachelor-Studiengang Physik und den Master-Studiengang Physik an der Universität Göttingen:

Hiermit erkläre ich, dass ich diese Abschlussarbeit selbständig verfasst habe, keine anderen als die angegebenen Quellen und Hilfsmittel benutzt habe und alle Stellen, die wörtlich oder sinngemäß aus veröffentlichten Schriften entnommen wurden, als solche kenntlich gemacht habe.

Darüberhinaus erkläre ich, dass diese Abschlussarbeit nicht, auch nicht auszugsweise, im Rahmen einer nichtbestandenen Prüfung an dieser oder einer anderen Hochschule eingereicht wurde.

Göttingen, den 29. Oktober 2020

(Yannik Buch)